CELLULAR NEUROSCIENCE

Calcium-activated ion channels drive atypical inhibition in medial habenula neurons

Takafumi Kawai[1,2], Ping Dong[1], Konstantin Bakhurin[3,4], Henry H. Yin[3,4], Huanghe Yang[1,3]*

Nicotine is an addictive substance that poses substantial health and societal challenges. Despite the known links between the medial habenula (MHb) and nicotine avoidance, the ionic mechanisms underlying MHb neuronal responses to nicotine remain unclear. Here, we report that MHb neurons use a long-lasting refractory period (LLRP) as an unconventional inhibitory mechanism to curb hyperexcitability. This process is initiated by nicotine-induced calcium influx through nicotinic acetylcholine receptors, which activates a calcium-activated chloride channel (CaCC). Owing to high intracellular chloride levels in MHb neurons, chloride efflux through CaCC, coupled with high-threshold voltage-gated calcium channels, sustains MHb depolarization near the chloride equilibrium potential of −30 millivolts, thereby enabling LLRP. Concurrently, calcium-activated BK potassium channels counteract this depolarization, promoting LLRP termination. Our findings reveal an atypical inhibitory mechanism, orchestrated by synergistic actions between calcium-permeable and calcium-activated channels. This discovery advances our understanding of neuronal excitability control and nicotine addiction.

INTRODUCTION

Tobacco smoking continues to be a substantial global public health challenge, responsible for millions of deaths every year (*1*). Nicotine, the primary addictive compound in tobacco, is at the center of smoking-induced health issues. Its impact is characterized by both rewarding and aversive effects, which are largely mediated by neuronal nicotinic acetylcholine receptors (nAChRs) (*2*–*5*). The self-administration of nicotine, observed in humans and rodents, follows an inverted U-shaped dose-response curve (*6*–*8*). Lower doses of nicotine are associated with rewarding effects that encourage consumption, while higher doses elicit aversive effects, promoting avoidance. This pattern highlights the complex neurobiological responses to varying levels of nicotine exposure. However, despite extensive research into this biphasic response to nicotine, the specific neuronal and circuit mechanisms driving the balance between nicotine's reward and aversion remain a subject of ongoing investigation.

The medial habenula (MHb), a compact bilateral nucleus located in the epithalamus of the diencephalon, is characterized by a high density of nAChRs, including the α5, α3, and β4 subunits encoded by the *CHRNA5-CHRNA3-CHRNB4* gene cluster (*2*, *3*). This particular gene cluster has been linked to an increased vulnerability to nicotine dependence, the intensity of smoking behaviors, and the susceptibility to smoking-related diseases (*4*). While the role of nAChRs in MHb neurons has been extensively studied (*6*, *9*–*13*), the precise manner in which these neurons react to varying nicotine concentrations and how they balance nicotine's rewarding and aversive effects continue to be subjects of ongoing debate.

Notably, MHb neurons exhibit unique electrophysiological properties that distinguish them from other adult central nervous system (CNS) neurons, including unusually high input resistance (*14*) and a distinct repertoire of ion transporters and channels (*15*–*19*). In addition to the abundant expression of nAChRs (*13*), these neurons prominently express the Cl^- importer $Na^+/K^+/Cl^-$ cotransporters (NKCCs) but lack the Cl^- extruder K^+/Cl^- cotransporter 2 (KCC2) (*16*, *17*). This imbalance leads to elevated intracellular Cl^- levels (~40 mM) and a high Cl^- equilibrium potential (E_{Cl}) of around −30 mV. Consequently, γ-aminobutyric acid type A ($GABA_A$) receptor activation, which typically hyperpolarizes mature neurons, depolarizes MHb neurons instead (*16*, *17*). Given the diverse excitatory inputs to the MHb (*4*, *14*, *16*, *17*, *20*–*22*), the nAChR-mediated membrane depolarization (*4*) and the high input resistance (*14*), an important question arises: How do MHb neurons acutely suppress hyperexcitability when strongly stimulated by nicotine?

In this study, by using both in vivo and ex vivo electrophysiology, we discovered that MHb neurons control the challenges of high-dose nicotine–induced hyperexcitability through an unconventional mechanism. Leveraging their inverted Cl^- gradient, MHb neurons orchestrate a synergistic response among nAChRs, calcium-activated chloride channels (CaCCs), and high-threshold voltage-gated calcium channels (VGCCs). This synergy triggers a positive feedback loop that sustains CaCC activation and stabilizes the MHb neuron's membrane potential near the E_{Cl}, leading to a long-lasting refractory period (LLRP) that can last minutes in vivo and has not been reported in any other brain regions, to our knowledge. We further demonstrated that BK channel–mediated K^+ efflux plays a crucial role in counterbalancing the sustained depolarization caused by CaCCs, thereby helping terminate the LLRP. Our findings thus illuminate a previously unknown electrophysiological property of MHb neurons, offering fresh insights into the neural mechanisms underlying nicotine addiction and avoidance.

RESULTS

Different doses of nicotine elicit distinct MHb neuronal responses in vivo

The MHb abundantly expresses nAChRs (*2*, *3*). While MHb responses to nicotine in vivo were recently investigated using calcium imaging via fiber photometry (*23*), the electrical responses of MHb neurons to varying concentrations of nicotine in vivo remain unexplored. To fill this knowledge gap, we implanted electrodes to the MHb and performed single-unit extracellular recordings of the MHb neurons from free-moving mice in vivo (Fig. 1, A and B). Saline

[1]Department of Biochemistry, Duke University Medical Center, Durham, NC 27710, USA. [2]Integrative Physiology, Graduate School of Medicine, Osaka University, Suita 565-0871, Japan. [3]Department of Neurobiology, Duke University Medical Center, Durham, NC 27710, USA. [4]Department of Psychology and Neuroscience, Duke University, Durham, NC 27708, USA.
*Corresponding author. Email: huanghe.yang@duke.edu

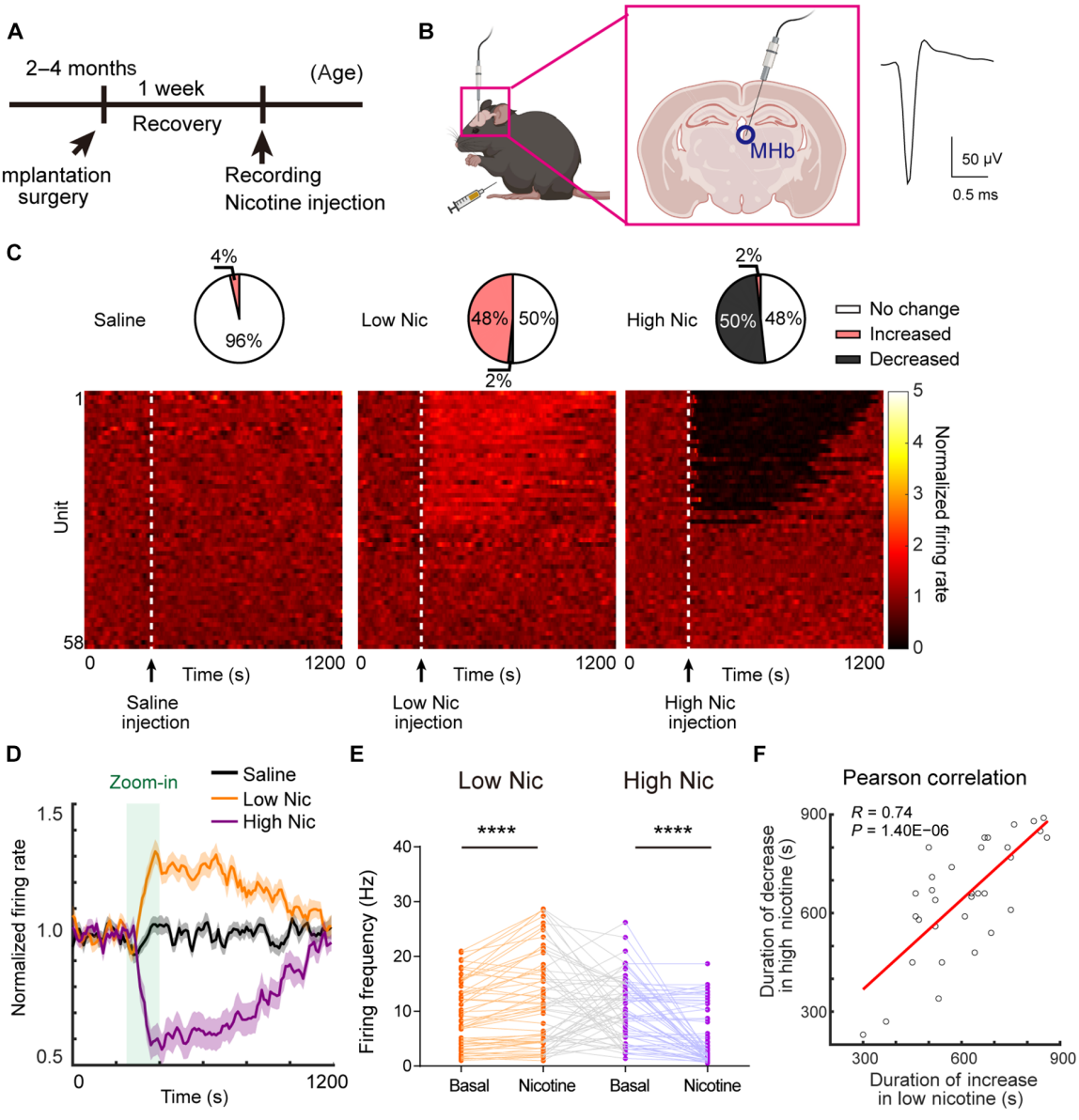

Fig. 1. Low-dose nicotine enhances yet high-dose nicotine suppresses the neural activities of MHb neurons in vivo. (**A**) Time frame for in vivo single-unit extracellular recording. (**B**) Schematic of in vivo single-unit extracellular recording. Representative waveform of single-unit signal is shown on the right. (**C**) Normalized firing rates of single-unit recordings in 58 MHb neurons from five different mice before and after saline (left), 0.1 mg/kg (low Nic, middle), and 0.5 mg/kg (high Nic, right) nicotine administration (intraperitoneally). All traces were aligned at the time of drug administration (dashed line). Pie charts (top) plot the percentages of neurons with increased, decreased, or no change of firing under each condition (see Materials and Methods for definitions). Time bin is 10 s. (**D**) Averaged firing rate of all 58 units in response to saline, 0.1 mg/kg, or 0.5 mg/kg nicotine administration. Firing rate changes were normalized to the basal firing rate before drug administration. Time bin is 10 s. The light green shaded range labels the time duration shown in fig. S1 (A and B). (**E**) Comparison of firing frequency before and during nicotine administration. Left: low nicotine; right: high nicotine. Each dot shows the averaged firing frequency of 50 to 100 s (basal) and 400 to 450 s (nicotine). $N = 58$. ****$P < 0.0001$. Paired t test. (**F**) Pearson correlation analysis of the single-unit signals that responded to sequential administration of 0.1 mg/kg (x axis) and 0.5 mg/kg nicotine (y axis, see details in Materials and Methods).

injection had negligible effect on the basal MHb neurons' firing frequency (10.3 ± 0.8 Hz, Fig. 1C). Low-dose administration [0.1 mg/kg, intraperitoneally (ip)], which is in the range of nicotine rewarding (*6*, *7*, *24*), markedly increased firing in ~50% of the recorded neurons (Fig. 1, C and D, with 10-s bins). This is consistent with the previous in vitro experiments that nicotine application enhances MHb neural activities (*3*, *9*, *25*). The remaining units that did not respond to nicotine likely recorded the dorsal MHb neurons that do not express nAChRs (*3*) or the neurons outside of the MHb due to the small size of the MHb.

In stark contrast, administration of the reported aversive dose of nicotine (0.5 mg/kg, ip) (*7*, *24*) did not lead to enhanced MHb firing. Instead, the overall firing from ~50% of the recorded neurons was suppressed for several minutes (Fig. 1, C and D, with 10-s binning). To investigate the identity of these neurons, we sequentially administered both low (0.1 mg/kg) and aversive (0.5 mg/kg) concentrations

of nicotine to the same animals. There was a strong correlation between the low nicotine–excited neurons and the high nicotine–inhibited neurons (Fig. 1, E and F). Most of the MHb neurons that increased firing in response to low nicotine also showed long silencing period after high nicotine administration. We also closely examined the initial phase (50 s before and 100 s after nicotine administration) of nicotine responses upon low- or high-dose administration (fig. S1, A and B, with 1-s binning). At 0.1 mg/kg dosage, a gradual increase in firing frequency was observed (fig. S1A with 1-s bins), whereas at 0.5 mg/kg dosage, a transient increase in firing frequency was readily observed 0 to 50 s postadministration followed by a rapid suppression of firing (fig. S1B, left, with 1-s binning). While no obvious single-unit spike waveform changes before, during, and after nicotine (0.5 mg/kg) administration (fig. S1D), the raster plot clearly shows an increase in firing followed by diminished firing (fig. S1C). This transient increase in firing frequency accounted for 89% of the neuronal population in which firing suppression was observed (fig. S1B, right). These observations under aversive dose of nicotine administration indicate that nicotine, a highly lipophilic compound (*26*, *27*), rapidly reaches the MHb and transiently excites MHb neurons followed by a sudden and prolonged inhibition that can last for minutes (Fig. 1, C and D).

Strong nicotine stimulation induces an LLRP in MHb neurons

To dissect the underlying mechanism of the concentration-dependent responses to nicotine, we conducted loose cell–attached (LCA) recordings of the ventral MHb neurons in acutely isolated brain slices ex vivo (Fig. 2, A and B). This configuration allowed us to closely examine the nicotine response of MHb neurons while keeping their intracellular environment including ion concentrations intact. A short focal puff of nicotine was administered to the ventral MHb, specifically the MHbVm and MHbVc. Similar to previous reports (*3*, *9*, *25*), a 5-s puff of 1 μM nicotine induced transient increase of firing frequency in the MHb neurons (Fig. 2, F to H), while a puff of artificial cerebrospinal fluid (aCSF), as a negative control, did not change MHb firing (Fig. 2, C to E). The 1 μM nicotine-induced firing increase was transient, and the neurons rapidly recovered to their basal firing rate after the puff was terminated (Fig. 2, F to H). In contrast, a stronger stimulation with 10 μM nicotine induced a transient increase in firing followed by an ultralong period of silent phase, during which no firing was observed even after the termination of the nicotine puff (Fig. 2, I to K). Of note, about 70% of the 16 recorded MHb neurons showed more than 30 s of silent phase (Fig. 2K, median value = 37 s).

To further understand the long-lasting silent phase, we used optogenetic stimulation after 10 μM nicotine puff (Fig. 3A). First, we prepared the brain slices from the ChAT-ChR2-eYFP mice, which express channelrhodopsin-2 (ChR2) fused with eYFP in cholinergic neurons including the ventral MHb neurons (*28*, *29*). Then, we excited the ChR2-experssing MHb neurons with a 2-s blue light stimulation in the absence of nicotine. There was a transient increase of firing rate, which rapidly recovered after light stimulation (Fig. 3, B to D, "Basal"). Next, we induced the silent phase with a 10 μM nicotine puff followed by the same blue light stimulation (Fig. 3, B to D, "Nicotine"). No spikes can be triggered during the silent phase, indicating that the neurons have entered a prolonged refractory period. After the MHb neurons recovered from the silent phase by washing off nicotine, the blue light stimulation can enhance the firing activity again (Fig. 3, B to D, "Recovery"). Together, our ex vivo results support in vivo observations that MHb neurons can have two distinct firing modes depending on the strength of nicotine stimulation. Milder nicotine increases their firing, yet stronger nicotine triggers an LLRP, during which the MHb neurons completely stop firing and no longer respond to excitatory inputs.

A Cl^- conductance dominates the LLRP

To dissect the ionic basis of the LLRP in MHb neurons, we performed current clamp recording under whole-cell configuration (Fig. 4A). The MHb neurons have high intracellular Cl^- due to the lack of KCC2 K^+/Cl^- cotransporter expression, which helps extrude Cl^- ions (*17*). Therefore, the intracellular Cl^- concentration was set to 40 mM with a reversal potential (E_{Cl}) of −31.7 mV (*14*, *17*). By adjusting the membrane potential via current injection, we maintained the neurons' spontaneous firing at a frequency similar to that observed in the LCA recordings, approximately 2 to 3 Hz (Fig. 2). Similar to our LCA recording, a 5-s puff of 1 μM nicotine induced a transient increase of firing in MHb neurons (Fig. 4, A and B), whereas 10 μM nicotine transiently enhanced MHb firing followed by a long-lasting silent phase even after the termination of nicotine application (Fig. 4C). During this phase, the neurons were clamped at a plateau potential around −30 mV, during which voltage-gated Na^+ channels (NaVs) are all inactivated (*30*).

We noticed that the 10 μM nicotine-induced plateau potential is close to the E_{Cl} (Fig. 4D), raising the possibility that a Cl^- conductance may dominate the plateau potential of LLRP. To test this hypothesis, we held the membrane potential at around −70 mV (to suppress spontaneous firing) and compared the MHb responses to 10 μM nicotine by varying $[Cl^-]_{in}$ to 80 mM (Fig. 4, D and E). Distinct from 40 mM $[Cl^-]_{in}$ under which condition 63% of the neurons showed the LLRP with a plateau potential of −32.7 ± 0.64 mV and a median duration (quantified the time above −40 mV) of 8.83 s [interquartile range (IQR), 6.95 to 11.81], 80 mM $[Cl^-]_{in}$ (E_{Cl} = −12.9 mV) markedly prolonged the LLRP duration to 93.67 s (IQR, 54.61 to 149.6) with a more depolarized plateau potential of −27.4 ± 1.27 mV in all MHb neurons. The dependence of the LLRP duration and plateau potential on $[Cl^-]_{in}$ thus suggests that a Cl^- conductance dominates the strong nicotine stimulation–induced LLRP.

A Ca^{2+}-activated Cl^- conductance is activated by nicotinic stimulation

Our voltage clamp recording of the MHb neurons detected a typical voltage- and time-dependent, outward rectifying CaCC current (fig. S2) (*31*). This current can be inhibited by including a nonselective Cl^- channel blocker niflumic acid (NFA) or a Ca^{2+} chelator EGTA in the patch pipettes, supporting the abundant expression of CaCC in MHb neurons (*18*). We thus hypothesize that the CaCC is responsible for the Cl^- conductance that sustains the LLRP.

To test this hypothesis, we measured the inward current of MHb neurons in response to 10 μM nicotine using voltage-clamp at the holding potential of −80 mV when all VGCCs are closed (Fig. 5A). With 2 mM extracellular Ca^{2+} ($[Ca^{2+}]_{out}$) and 140 mM intracellular Cl^- ($[Cl^-]_{in}$), the nicotine-induced inward current showed three phases, an instantaneous current (a) followed by a growing phase (b) during the nicotine puff and a slow decaying phase (c) after terminating the nicotine puff (Fig. 5B). Increasing $[Ca^{2+}]_{out}$ from 2 to 5 mM significantly boosted the instantaneous current (Fig. 5, C and E), which may be due to augmented Ca^{2+} influx under this condition. In addition, the growing phase was also significantly enhanced (Fig. 5, C and F) and the slow decaying phase became markedly prolonged (Fig. 5, C and G).

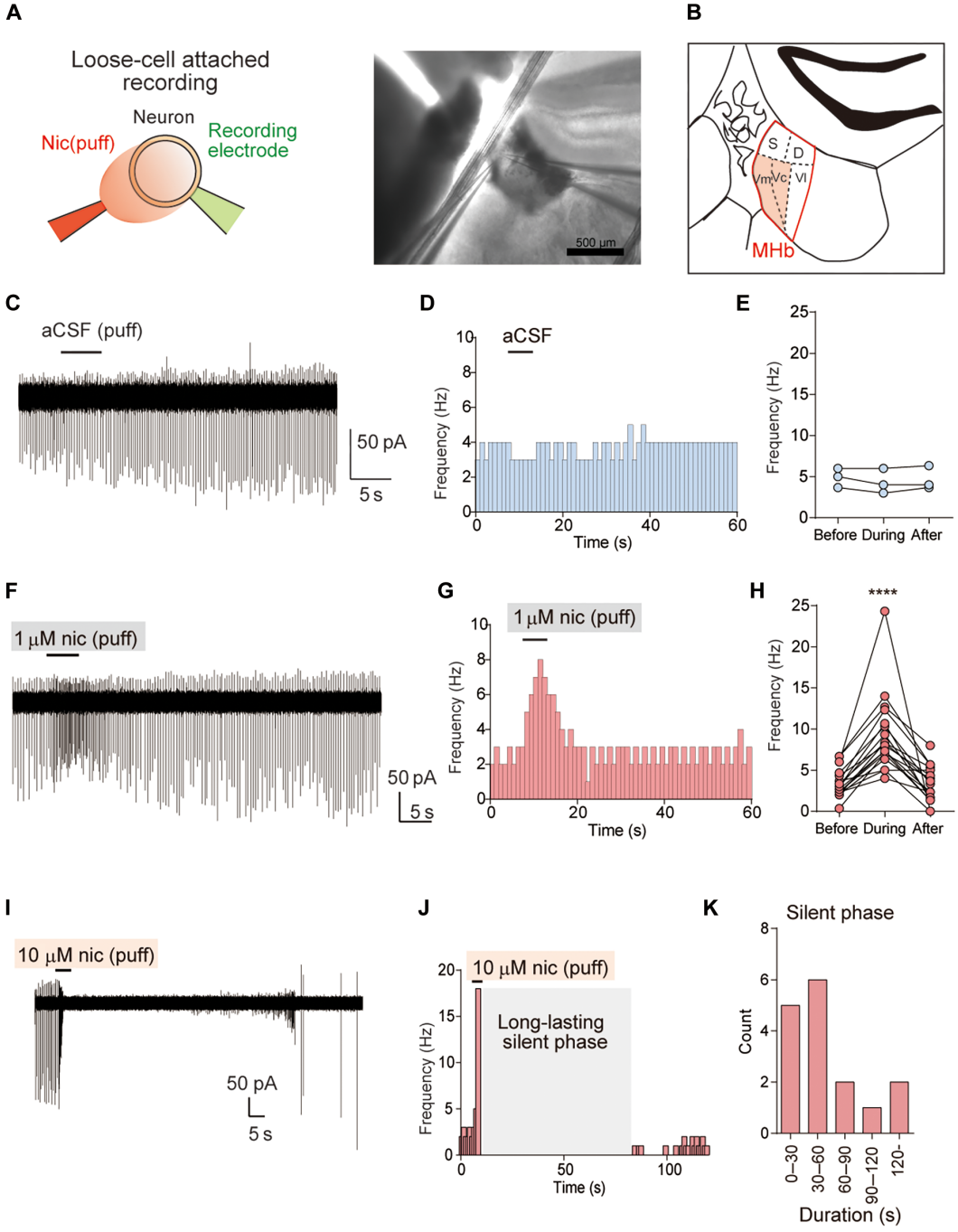

Fig. 2. Low-dose nicotine enhances MHb firing yet high-dose nicotine forces MHb neurons into a long-lasting silent phase. (**A**) Schematic (left) and a representative photograph (right) of ex vivo LCA recording. Left pipette delivers nicotine; right electrode records electrical signal. (**B**) A coronal section of the MHb showing the slice recording locations. Dorsal (MHbD), superior (MHbS), ventral medial (MHbVm), ventral central (MHbVc), and ventral lateral (MHbVl) are shown as D, S, Vm, Vc, and Vl, respectively. The pink-shaded MHbVm and MHbVc are investigated in the present study. (**C**) A representative LCA trace of MHb firing in response to a 5-s puff of aCSF. (**D**) Peristimulus time histogram (PSTH) of MHb firing frequency in response to a 5-s puff of aCSF. The firing frequency was binned at 1-s interval. (**E**) The comparison of MHb firing frequency before, during, and after the aCSF puff ($n = 3$). (**F**) A representative LCA trace of MHb firing in response to a 5-s puff of 1 μM nicotine. (**G**) PSTH of MHb firing frequency in response to a 1 μM nicotine puff. (**H**) The comparison of MHb firing frequency before, during, and after the 1 μM nicotine puff ($n = 18$, $^{****}P < 0.0001$, Dunn's multiple comparisons). (**I**) A representative trace of MHb firing in response to a 5-s puff of 10 μM nicotine. (**J**) PSTH of MHb firing frequency in response to a 10 μM nicotine puff. Note a long silent phase following 10 μM nicotine administration. (**K**) Distribution histogram of the silent phase durations from MHb neurons with 30-s binning. $N = 16$.

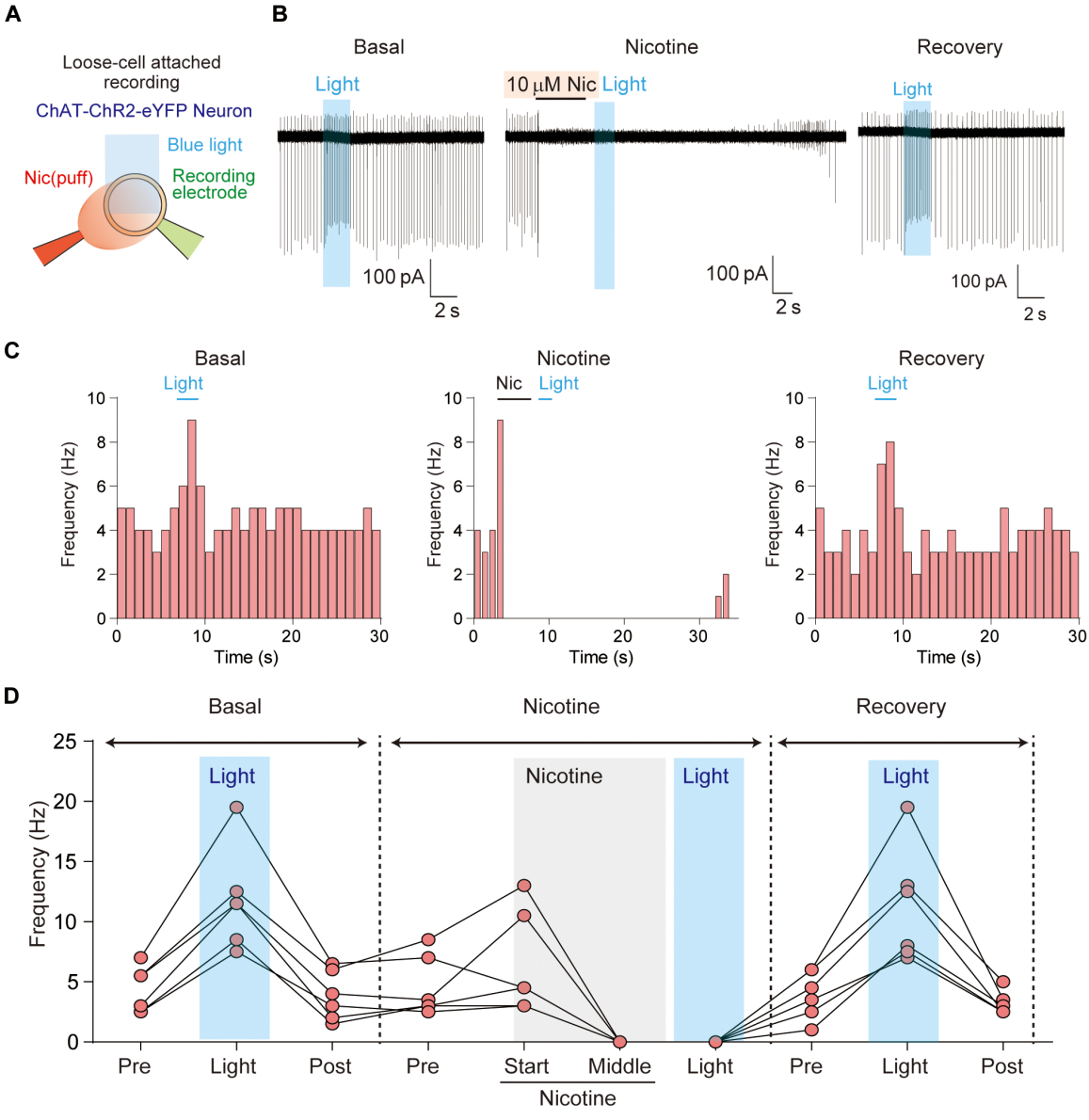

Fig. 3. High-dose nicotine induces an LLRP in MHb neurons. (**A**) Schematic of LCA recording with optogenetic stimulation. (**B**) Representative LCA traces of a ChR2-expressing MHb neuron from a ChAT-ChR2-eYFP mouse in response to blue light stimulation (cyan). Left: basal activity; middle: with 10 μM nicotine; right: after washing off nicotine. (**C**) Corresponding PSTHs in (B). (**D**) Summary of firing frequency changes from the same MHb neurons in response to light illumination before (basal), during (nicotine), and after (recovery) 10 μM nicotine administration. "Start" in nicotine application indicates the firing frequency in the first 1 s during nicotine application, whereas "middle" indicates that of 2.5 to 3.5 s during nicotine application. $n = 6$ neurons.

On the other hand, adding 5 mM EGTA in the intracellular pipette solution abolished the growing phase during the nicotine puff without obviously affecting the nicotine-induced instantaneous current (Fig. 5, D and E). The charge flow during this phase was also significantly reduced (Fig. 5, D and G). On the basis of all these, we conclude that the instantaneous current is mainly derived from cation influx through nAChRs. The nAChR-mediated Ca^{2+} entry then activates the CaCC during the nicotine puff. CaCC-mediated Cl^- efflux further enhances the inward current (Fig. 5F). The CaCC continues to open for a prolonged period even after the nicotine puff stops, giving rise to the slow decaying phase (Fig. 5G) that prolongs when $[Ca^{2+}]_{out}$ increases (Fig. 5C) and diminishes when intracellular EGTA chelates Ca^{2+} influx (Fig. 5D). Decreasing intracellular Cl^- from 140 to 5 mM effectively eliminates the growing phase and suppresses the decaying phase (fig. S3). This demonstrates that the driving force for CaCC-mediated Cl^- efflux is essential for maintaining the growing phase and the decaying phase, further supporting that high nicotine-mediated Ca^{2+} influx activates the slow decaying inward CaCC current for a prolonged period. Taking our current clamp and voltage clamp results together, we conclude that high nicotine stimulation activates a slow decaying inward CaCC current that mediates the long-lasting membrane depolarization toward the E_{Cl}. As the physiological E_{Cl} for MHb neurons is near −30 mV (*14*), high nicotine–induced CaCC opening thus inactivates NaVs and forces the neurons to enter LLRP.

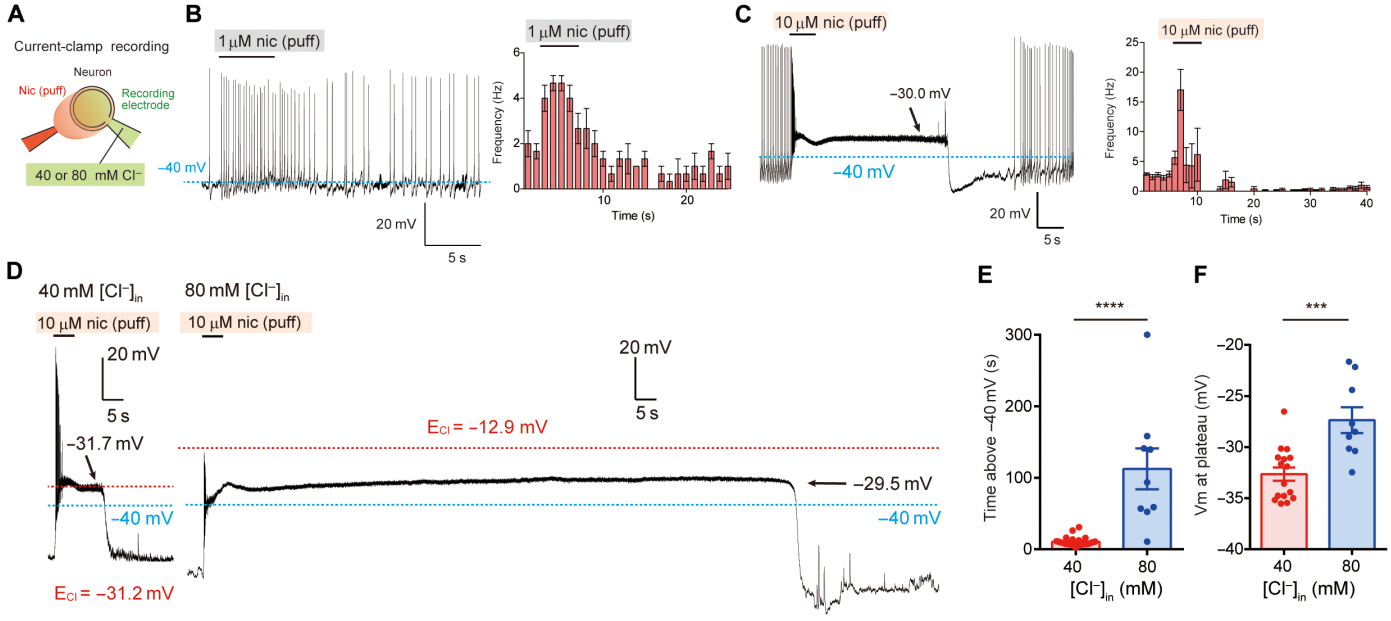

Fig. 4. A Cl^- conductance dominates the high-dose nicotine–induced LLRP in MHb neurons. (**A**) Schematic of ex vivo whole-cell current clamp recording. (**B**) Left: A representative trace of MHb current clamp recording before, during, and after 1 μM nicotine puff. Membrane potential was held ~−40 mV to enable spontaneous firing (2 to 3 Hz). Right: Peristimulus time histogram (PSTH) of MHb firing frequency in response to a 5-s puff of 1 μM nicotine. The firing frequency was binned at 1-s interval. $n = 3$ neurons. (**C**) Left: A representative trace of MHb current clamp recording before, during, and after 10 μM nicotine puff. Right: PSTH of MHb firing frequency in response to a 5-s puff of 10 μM nicotine. The firing frequency was binned at 1-s interval. $n = 8$ neurons. (**D**) Representative traces of MHb current clamp recording in response to a 10 μM nicotine puff with 40 mM (left) and 80 mM (right) intracellular Cl^- ($[Cl^-]_{in}$). The membrane potential was held at ~−70 mV to suppress spontaneous firing. E_{Cl} and −40 mV were indicated by red and cyan dotted lines, respectively. (**E**) Statistical comparison of the durations above −40 mV for recordings with 40 and 80 mM $[Cl^-]_i$. We set the upper limit at 300 s. ****$P < 0.0001$. Mann-Whitney U test. $n = 25$ and 9 for 40 and 80 mM $[Cl^-]_{in}$, respectively. (**F**) Statistical comparison of the membrane potentials at the plateau phase with 40 and 80 mM $[Cl^-]_i$. ***$P < 0.001$, t test. $N = 16$ and 9 for 40 and 80 mM $[Cl^-]_{in}$, respectively.

TMEM16A is likely the CaCC to sustain MHb LLRP

Having identified the importance of CaCC in LLRP, we attempted to pinpoint the molecular identity of the CaCC. Recent studies showed that TMEM16A, a canonical CaCC with voltage- and time-dependent outward rectifying current under submicromolar Ca^{2+} (*32*–*36*), is highly expressed in the MHb (*15*, *32*). Therefore, we hypothesized that TMEM16A is likely responsible for the MHb CaCC (fig. S2). To test this, we tested the effects of CaCCinh-A01, a TMEM16A-specific inhibitor (*37*, *38*), on the MHb CaCC current and the nicotine-induced LLRP. We found that 10 μM extracellular CaCCinh-A01 abolishes both the outward rectifying peak current and the slowly deactivating tail current (Fig. 6, A and B). In addition, 10 μM CaCCinh-A01 also significantly diminishes the 10 μM nicotine-induced LLRP under 80 mM $[Cl^-]_{in}$ (Fig. 6, C and D). Our pharmacological findings using a TMEM16A inhibitor strongly support that the activation of TMEM16A, the highly expressed CaCC in the MHb (*15*, *32*), is crucial for the maintenance of LLRP.

Positive feedback loop between CaCC and VGCCs sustains the LLRP

The high nicotine–induced, long-lasting plateau potential maintains at approximately −30 mV (Fig. 4C). Under this voltage range, high-threshold VGCCs starts to be maximally activated (*30*). As shown in fig. S2, depolarization-induced Ca^{2+} entry through VGCCs robustly activates MHb CaCCs. We thus hypothesized that VGCCs may further promote MHb CaCC activation and positively contribute to the LLRP. To test this hypothesis, we applied various types of VGCC inhibitors to MHb neurons and quantified their effects on the high nicotine–induced LLRP (Fig. 7). The intracellular $[Cl^-]_{in}$ was set at 80 mM to promote the long-lasting plateau potential (Figs. 4E and 7, A and B). When we applied 200 μM $CdCl_2$, a pan-VGCC blocker, to the MHb neurons, the long-lasting plateau phase was abolished (Fig. 7, C and G), suggesting that MHb VGCCs indeed plays a key role in promoting CaCC opening during the long-lasting plateau potential. Previous studies show that both L- and R-type high-threshold VGCCs (HVA) and T-type low-threshold VGCCs (LVA) are expressed in MHb neurons (*39*, *40*). To further dissect the identities of VGCCs that contribute to the plateau potentials, we applied more specific VGCC inhibitors. We found that either 1 μM nifedipine (an L-type VGCC inhibitor) or 200 nM SNX-482 (an R-type VGCC inhibitor) significantly shortened the duration of the LLRP (Fig. 7, D, E, and G). On the other hand, the LLRP duration in the presence of 10 μM TTA-P2 (a T-type VGCC inhibitor) is comparable to the control group (Fig. 7, F and G). These results indicate that at the plateau potential of ~−30 mV that is induced by high nicotine stimulation and subsequent CaCC activation, the opening of L-type and R-type HVA VGCCs provides additional Ca^{2+} entry that prolongs CaCC opening. The positive feedback between CaCCs and HVA VGCCs in turn helps maintain the plateau potential that inactivates NaVs, leading to an LLRP. On the other hand, T-type LVA VGCCs, which completely inactivate at this voltage (*30*), play a negligible role in sustaining the LLRP.

BK K^+ channels help terminate the LLRP

We next questioned how the positive feedback loop between CaCC and the HVA VGCCs is broken and the LLRP terminates. In neurons,

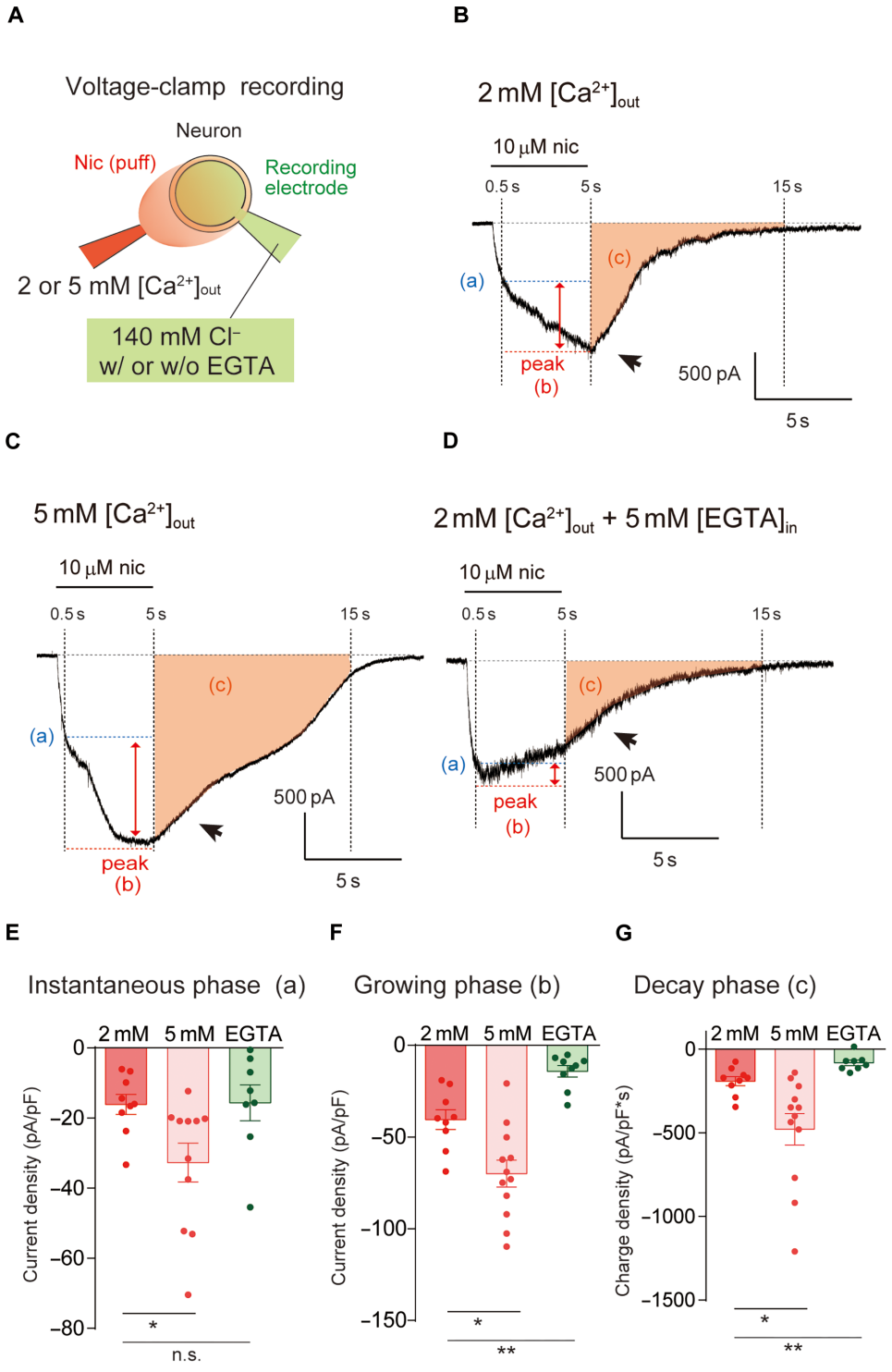

Fig. 5. A Ca^{2+}-activated Cl^- conductance (CaCC) is activated by high-dose nicotine stimulation in MHb neurons. (**A**) Schematic of ex vivo whole-cell voltage clamp recording. (**B** to **D**) Representative whole-cell voltage-clamp recording in response to a 5-s puff of 10 μM nicotine with 2 mM extracellular Ca^{2+} {$[Ca^{2+}]_{out}$, (B)}, 5 mM $[Ca^{2+}]_{out}$ (C), and 2 mM $[Ca^{2+}]_{out}$ + 5 mM intracellular EGTA {$[EGTA]_{in}$, (D)}. Symmetric $[Cl^-]$ (140 mM) was used, and the membrane voltage was held at −80 mV to prevent VGCC activation. The 10 μM nicotine-induced inward current has three phases: an instantaneous phase (a), a growing phase (b), and a decay phase (c). (**E** to **G**) Comparison of the high-dose nicotine–induced current during the instantaneous phase [the current density at 0.5 s of nicotine administration (E)], the growing phase [the peak current density between 0.5 and 5 s of nicotine administration (F)], and the decay phase [the charge density or the area under the curve between 5 and 15 s after nicotine administration (G)] under the three different conditions in (B) to (D). Multiple comparisons *t* test with Bonferroni correction was performed between 2 mM $[Ca^{2+}]_{out}$ and the other two conditions. *$P < 0.05$; ** $P < 0.01$. n.s., not significant. $n = 9$, 12, and 9 for 2 mM $[Ca^{2+}]_{out}$, 5 mM $[Ca^{2+}]_{out}$, and 2 mM $[Ca^{2+}]_{out}$ + 5 mM $[EGTA]_{in}$, respectively. Outliers were removed by detecting with the ROUT method (*65*).

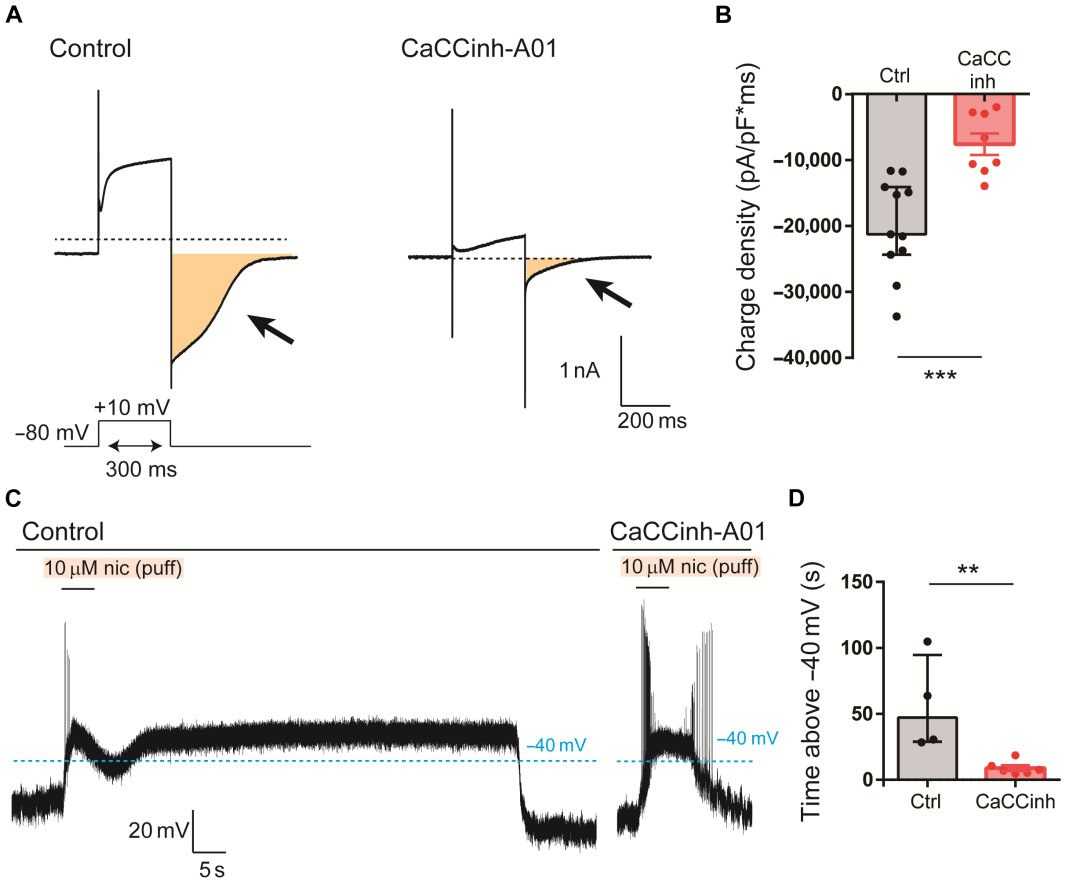

Fig. 6. TMEM16A inhibitor CaCCinh-A01 attenuates MHb CaCC current and suppresses LLRP. (**A**) Representative whole-cell CaCC current traces without (Control) and with 10 μM CaCCinh-A01. The membrane potential was changed from the holding potential of −80 to +10 mV to activate VGCC. Ca^{2+} increase through VGCC activity and the +10 mV depolarization open MHb CaCCs (*66*), resulting in the typical time-dependent, outward-rectifying CaCC peak current followed by a slow deactivating CaCC tail current (arrows) when the membrane voltage returns to the holding potential at −80 mV. The dotted line indicates zero current. (**B**) Statistical analysis of CaCC tail current. Five seconds of the tail current was measured for charge intensity, which is shown with orange in (A). ***$P < 0.001$, *t* test. $n = 11$ and 9 for control and CaCCinh-A01, respectively. (**C**) Representative traces of MHb current clamp recording in response to a 10 μM nicotine puff with (right) or without (left) 10 μM CaCCinh-A01. The experiments were done with 80 mM $[Cl^-]_{in}$. The membrane potential was held at ~−70 mV. −40 mV was indicated by cyan dotted lines. The trace is post hoc filtered with a 500-Hz low-pass filter. (**D**) Statistical comparison of the durations above −40 mV for control and CaCCinh-A01. **$P < 0.01$. Mann-Whitney *U* test. $n = 4$ and 6 for control and CaCCinh-A01, respectively.

Ca^{2+}- and voltage-activated BK large conductance K^+ channels, the opening of which leads to K^+ efflux and membrane hyperpolarization (*41*), are well known to effectively limit HVA VGCC-mediated Ca^{2+} influx through a negative feedback mechanism (*41*, *42*). Consistent with previous reports (*15*, *43*, *44*), the pore-forming α subunit of BK channel encoded by *Kcnma1* is highly expressed in the MHb (Fig. 8A, top). We therefore hypothesized that BK-mediated membrane hyperpolarization may counteract CaCC-induced depolarization, facilitating the termination of high nicotine–induced LLRP. To test this hypothesis, we first measured the nicotine-triggered LLRP in the MHb neurons from the *Kcnma1* deficient (BK KO) mice. Our immunohistochemistry result demonstrated that BK is absent from the KO MHb (Fig. 8A, bottom). Consistent with our hypothesis, the LLRP of the BK KO neurons is significantly longer than the littermate wild-type (WT) controls (Fig. 8, B and C). In addition, we treated the MHb slices from C57/BL6J mice with 10 μM paxilline (Fig. 8D), a BK channel–specific blocker (*45*). We found that BK pharmacological inhibition also significantly prolonged the plateau phase (Fig. 8, E and F). Paxilline depolarizes the plateau potential to −26.64 ± 0.84 mV, which is much higher than the plateau voltage of −32.64 ± 0.80 mV without BK inhibition (Fig. 8G). These genetic and pharmacological inhibition experiments collectively suggest that BK channels are activated during the LLRP, presumably downstream of the HVA VGCCs that usually form protein complexes with BK channels (*42*). The large K^+ conductance of BK channels thereby efficiently hyperpolarizes the membrane and subsequently shortens the duration of the LLRP.

We further dissect BK channel's role in regulating the LLRP using our BK D434G channelopathy mouse model, which carries a gain-of-function (GOF) mutation derived from human patients with generalized absence epilepsy and concurrent paroxysmal dyskinesia (*45*–*47*). We hypothesized that BK-D434G GOF in the MHb neurons would exert an opposite effect from BK inhibition on the LLRP induced by 10 μM nicotine. We found that the MHb neurons from the heterozygous mice ($BK^{DG/WT}$) barely could develop the LLRP seen in the WT ($BK^{WT/WT}$) MHb neurons (Figs. 8H, left and middle, and 7I). After transient spikes, the $BK^{DG/WT}$ MHb neurons rapidly hyperpolarized toward voltages below −40 mV even in the presence of nicotine stimulation. This suggests that the GOF BK

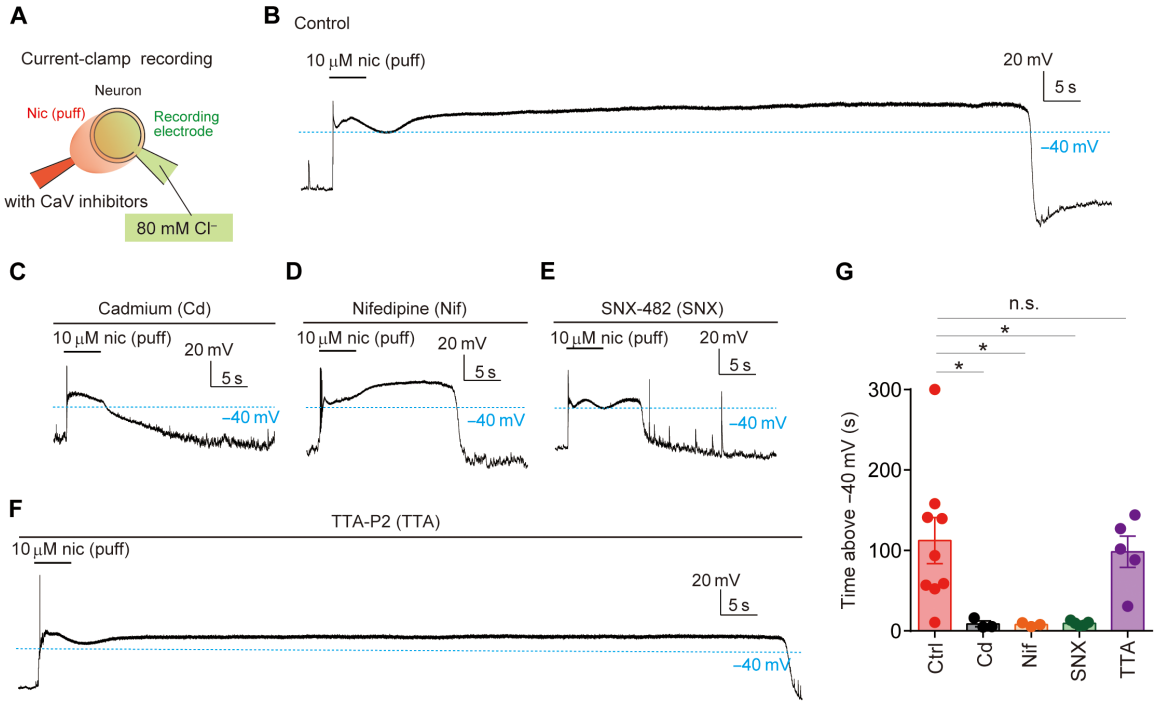

Fig. 7. The positive feedback between high-threshold voltage-gated Ca^{2+} channels (HVA-VGCCs) and Ca^{2+}-activated Cl^- channels (CaCCs) sustains the LLRP in MHb neurons. (**A**) Schematic of the ex vivo whole-cell current clamp recording. (**B** to **F**) Representative whole-cell current clamp recordings of MHb neurons in response to 10 μM nicotine under control (B), 200 μM pan-VGCC blocker $CdCl_2$ (C), 1 μM L-type VGCC inhibitor nifedipine (D), 200 nM R-type VGCC inhibitor SNX-482 (E), and 10 μM T-type VGCC TTA-P2 (F). The resting membrane potential was held around −70 mV, and $[Cl^-]_{in}$ was set at 80 mM to enhance the high-dose nicotine–induced LLRP. (**G**) Summary of the duration of the 10 μM nicotine-induced refractory period in MHb neurons in response to aCSF control (Ctrl), $CdCl_2$ (Cd), SNX-482 (SNX), nifedipine (Nif), and TTA-P2 (TTA). We set the upper limit at 300 s. Dunn's multiple comparison test. $^*P < 0.05$. n.s., not significant. $n = 11$, 3, 5, 4, and 6 for control, Cd, SNX, Nif, and TTA, respectively.

channel is also activated by nicotine-induced Ca^{2+} entry and membrane depolarization, and its large K^+ conductance overrides CaCC-mediated depolarization and prevents the formation of the CaCC-VGCC positive feedback. It is worth noting that BK GOF-mediated hyperpolarization also enables deinactivation of NaVs, as evidenced by the recovery of spontaneous spikes after nicotine stimulation (Fig. 8H, middle). Inhibition of BK D434G with paxilline successfully rescued the nicotine-induced LLRP, which is significantly longer than the LLRP from the $BK^{WT/WT}$ MHb neurons (Fig. 8, H, right, and I). Together, our findings with BK inhibition and potentiation explicitly demonstrate that BK channels in the MHb neurons actively regulate the LLRP and its enhanced activity facilitates LLRP termination.

DISCUSSION

Our in vivo and ex vivo experiments uncover that MHb neurons have a cell-autonomous machinery to differentially respond to different dosages of nicotine. By dissecting the ionic basis of this machinery, our findings shine light on understanding the complicated nicotine responses and helping establish novel targets to treat nicotine addiction.

We observed that weak nicotine stimulation increases MHb neuronal firing, whereas an aversive dose suppresses activity in vivo (Fig. 1). The low nicotine–induced excitatory effect is likely through nAChR-mediated Na^+ influx, which depolarizes the membrane and directly activates MHb NaV channels (Fig. 9, left). Under this condition, nAChRs may have limited Ca^{2+} permeability; thus, the abundantly expressed CaCC and BK channels are not engaged. In contrast, aversive nicotine doses induce an unconventional mechanism of limiting hyperexcitability in MHb neurons (Fig. 9, top right). MHb firing first transiently increases in response to strong nicotine stimulation, followed by a previously unknown LLRP, which serves as an emergency break to cease MHb firing. The transient increase of MHb firing is likely due to augmented cation influx through nAChRs, which depolarizes the MHb neurons and activates their NaVs. Concurrently, strong nicotine stimulation also leads to Ca^{2+} influx through nAChRs (*48*, *49*). This Ca^{2+} influx appears to directly activate CaCC (Fig. 5), because the observed nicotine-induced ion current mostly depended on the intracellular Cl^- (fig. S3) and there is no obvious expression of other Ca^{2+}-activated cation channels such as TRPM4 and TRPM5 in MHb (Allen Mouse Brain Atlas, https://mouse.brain-map.org).

nAChR-mediated Ca^{2+} increase and depolarization rapidly activate the CaCCs, whose opening requires both Ca^{2+} and voltage (fig. S1) (*35*, *50*). Owing to MHb neurons' high intracellular Cl^-, CaCC-mediated Cl^- efflux strongly depolarizes the membrane toward an E_{Cl} of −30 mV. This leads to the establishment and maintenance of the positive feedback between the CaCC and the HVA VGCCs. At this voltage range, HVA-VGCCs open without significant inactivation (*30*). Therefore, Ca^{2+} influx through the HVA-VGCCs can further depolarize MHb and activate more CaCCs, resulting in sustained

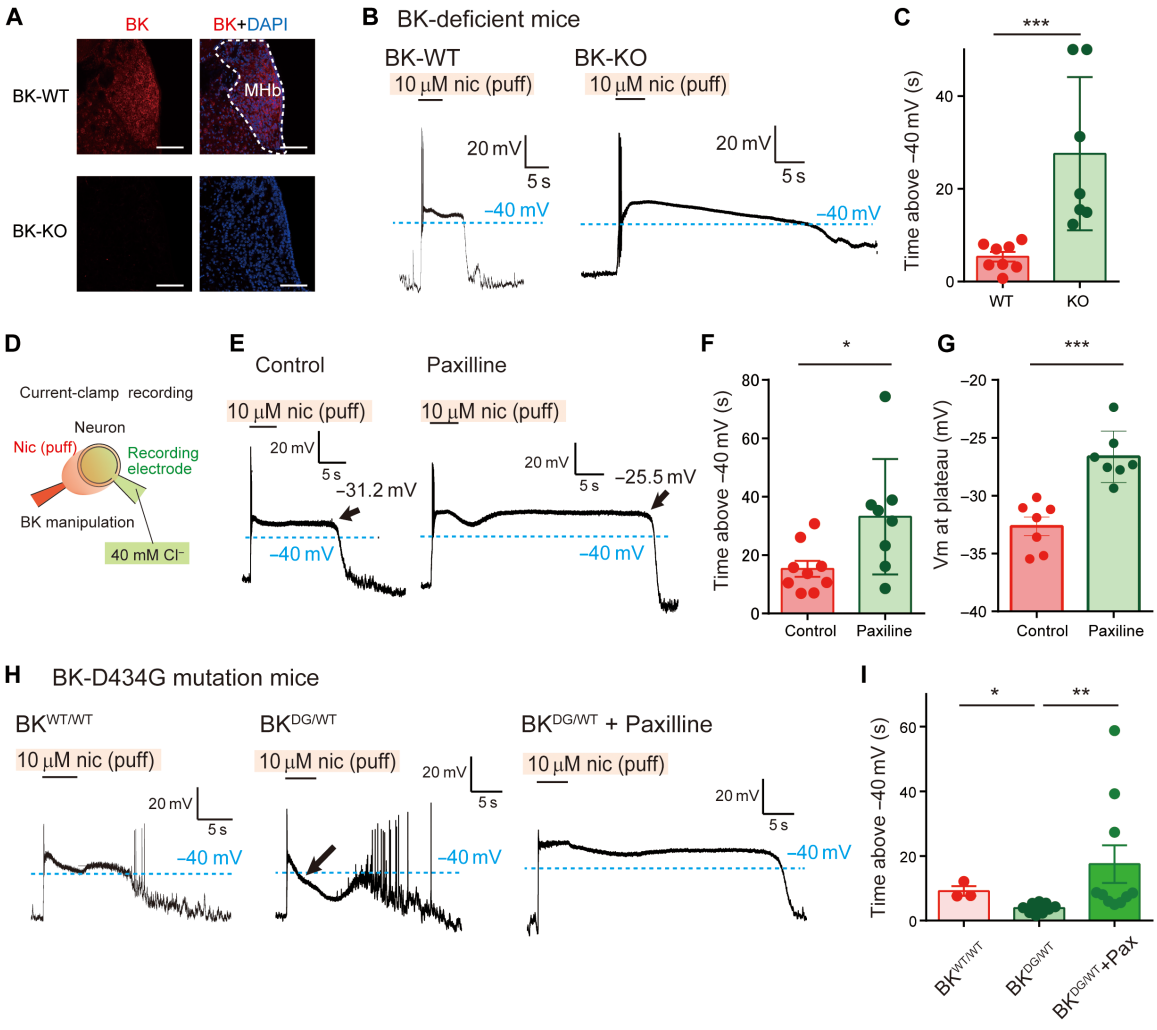

Fig. 8. BK channel negatively regulates the LLRP in MHb neurons. (**A**) Immunofluorescence of anti-Kcnma1 (red) for the MHb from BK wild-type (WT) and knockout (KO) mice. Blue: DAPI. Scale bar, 100 μm. (**B**) Representative whole-cell current clamp traces from the BK-WT and BK-KO MHb in response to 10 μM nicotine. The recordings were performed with 40 mM $[Cl^-]_{in}$, and the resting membrane potential was held around −70 mV by current injection. (**C**) Statistical comparison of the duration above −40 mV between BK-WT and BK-KO MHb neurons. We set the upper limit at 50 s. ***$P < 0.001$, Mann-Whitney *U* test. $N = 8$ and 7 for BK-WT and BK-KO, respectively. (**D**) Schematic of ex vivo whole-cell current clamp recording with BK inhibitor paxilline. The recordings were performed with 40 mM $[Cl^-]_{in}$ and the resting membrane potential was held around −70 mV by current injection. (**E**) Representative whole-cell current clamp traces with or without paxilline. (**F**) Statistical comparison of the duration above −40 mV between the control and paxilline treatment groups. *$P < 0.05$, Mann-Whitney *U* test. $N = 9$ and 8 for control and paxilline, respectively. (**G**) Statistical comparison of the membrane potential at the plateau phase. ***$P < 0.001$, *t* test. $N = 7$ and 7 for control and paxilline, respectively. (**H**) Representative whole-cell current clamp traces of the MHb neurons from WT ($BK^{WT/WT}$, left) and heterozygous BK-D434G ($BK^{DG/DG}$) mice without (middle) and with paxilline (right). (**I**) Statistical comparison of the duration above −40 mV among $BK^{WT/WT}$, $BK^{DG/WT}$, and $BK^{DG/WT}$ + paxilline treatment. *$P < 0.05$; **$P < 0.01$. Dunn's multiple comparison test. $N = 3$, 9, and 10 for $BK^{WT/WT}$, $BK^{DG/WT}$, and $BK^{DG/WT}$ + paxilline, respectively.

membrane depolarization, prolonged NaV inactivation, and the LLRP. Consistent with the LLRP observed in our in vitro experiments, our single-unit recording in freely moving animals also demonstrates that adverse doses of nicotine induce prolonged silence in vivo, which can last for minutes (Fig. 1, C and D). Although information on nicotine concentration in the brain following in vivo administration is limited, it has been reported that in rats, a dose of just 0.3 mg/kg can result in brain nicotine concentrations in the micromolar range even 30 min after injection (*51*). Similarly, in mice, a dose of 1.0 mg/kg has been observed to increase brain nicotine levels to nearly 10 μM (*52*). On the basis of this, we believe that the nicotine levels in our in vivo experiments fall within a similar range to those observed in ex vivo studies.

The regulatory effects of BK inhibition and potentiation on the duration of the LLRP strongly support that this Ca^{2+}- and voltage-activated K^+ channel is also actively involved in the LLRP (Fig. 8). Because BK channels have lower Ca^{2+} and voltage sensitivity compared with those of the canonical CaCCs (*35*, *41*, *50*, *53*, *54*), BK-mediated hyperpolarization is rather limited during the initiation and the early phase of the LLRP. During this period, the positive feedback between CaCCs and HVA VGCCs dominates, resulting in a plateau voltage near E_{Cl} (Fig. 9, top right). With the prolongation of the LLRP and more HVA VGCC opening, BK channels start to gain more weight on counterbalancing the depolarization induced by the CaCC-VGCC positive feedback, preventing the MHb membrane from becoming more depolarized. With nicotine dissociation,

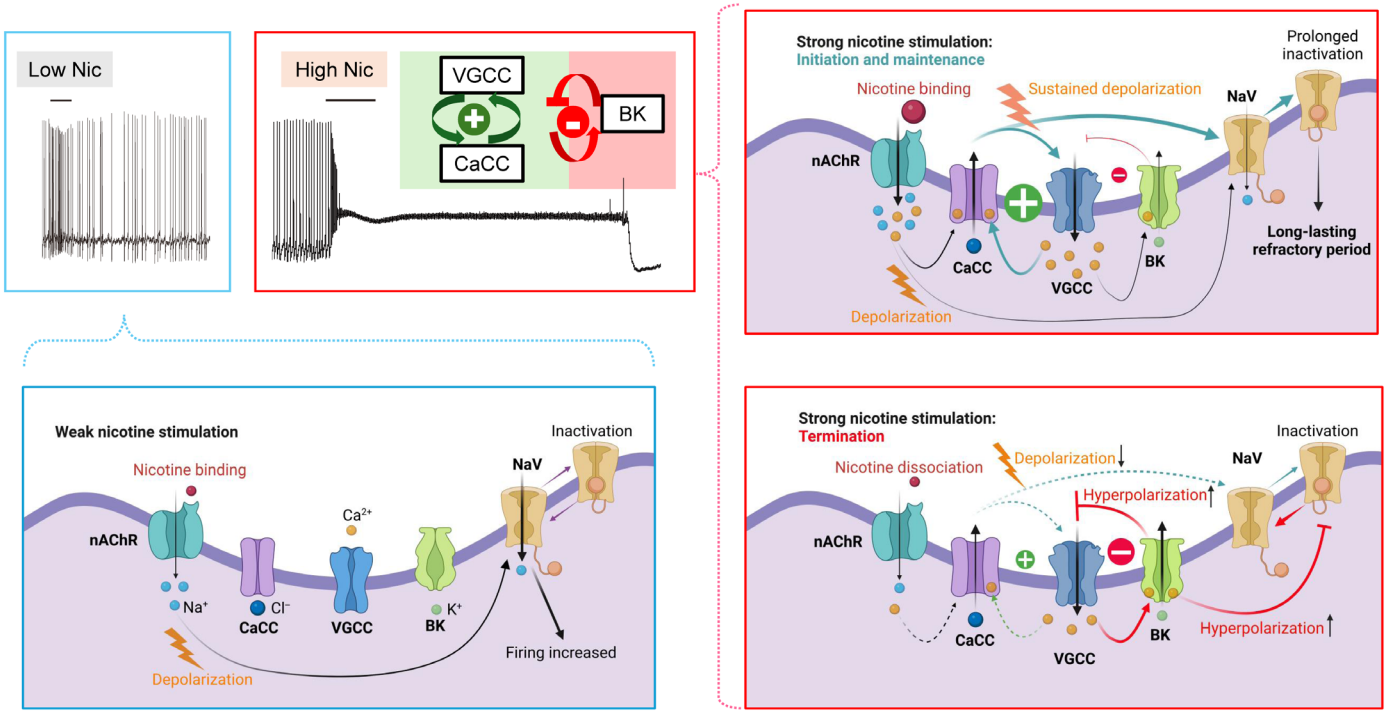

Fig. 9. A mechanistic model to depict the ionic basis of the MHb biphasic responses to nicotine. (Left, blue) Upon low nicotine (Nic) stimulation, the cation influx through the MHb nAChRs depolarizes the membrane, activates voltage-gated sodium channels (NaVs), and increases firing. **(Right, red)** High aversive levels of Nic strongly stimulate the MHb nAChRs, leading to transient NaV opening and firing increase. Concurrently, robust Ca^{2+} influx through the nAChRs activates Ca^{2+}-activated Cl^- channels (CaCCs), which further depolarizes the membrane to open the high-threshold VGCCs. The positive feedback loop between the CaCCs and the HVA-VGCCs promotes membrane depolarization around E_{Cl}, leading to sustained NaV inactivation and the LLRP (LLRP, top). In response to prolonged membrane depolarization and Ca^{2+} influx, Ca^{2+}-activated BK K^+ channels increasingly hyperpolarize the membrane, which negatively regulates the CaCC-HVA-VGCC positive feedback loop and promotes NaV deinactivation, facilitating the termination of the LLRP.

the CaCC-VGCC positive feedback gradually diminishes, and the enhanced BK-VGCC negative feedback ultimately introduces stronger membrane hyperpolarization, which contributes to the termination of the LLRP (Fig. 9, bottom right).

MHb neurons receive both glutamatergic input from the posterior septum and GABAergic input from the medial septum/diagonal band of Broca (*14*, *20*–*22*). Unlike most adult neurons in the CNS, MHb neurons lack an intrinsic $GABA_A$-dependent mechanism to rapidly mitigate hyperexcitability following intense stimulation (*16*, *17*). This is because MHb neurons' high intracellular Cl^- concentration determines that the MHb $GABA_A$ Cl^- channels are excitatory rather than inhibitory (*14*). Furthermore, glycine derived from astrocytes can also excite MHb neurons via atypical glycine-gated GluN1/GluN3A NMDA receptors (*55*). Given the high input resistance of MHb neurons (*14*), MHb neurons can be easily excited by these different types of excitatory inputs. How to rapidly curb MHb hyperexcitability, reduce hyperexcitability-induced damage, and relay hyperexcitability to its downstream brain regions is therefore a critical task that MHb neurons need to handle. The LLRP uncovered in this study, orchestrated by the synergistic actions of nAChRs, CaCCs, and HVA VGCCs, provides a cell-autonomous mechanism to rapidly cease MHb firing by clamping their membrane potential to a level where NaVs are inactivated (Fig. 9, top right). This unusual mechanism enables MHb neurons to swiftly shunt themselves from inputs from other brain regions, as evidenced by our in vivo single-unit recording in response to adverse doses of nicotine (Fig. 1). The LLRP should block the MHb neurons to relay their inputs to its primary downstream target, the interpeduncular nucleus (IPN). Future research will be needed to elucidate the LLRP's specific role in the MHb-IPN circuitry and in mediating responses to nicotine aversion.

We show that the Ca^{2+}- and voltage-activated CaCC and BK channels play a crucial role in the development and maintenance of the MHb LLRP. The MHb CaCC current is activated by Ca^{2+} and membrane depolarization and exhibits time-dependent activation and deactivation kinetics under physiological conditions. These are the hallmarks of canonical CaCCs that are encoded by *TMEM16A*/*ANO1* and *TMEM16B*/*ANO2* (*31*). According to recent studies, TMEM16A but not TMEM16B is highly expressed in the majority of ventral MHb neurons (*15*, *32*), where we conducted our ex vivo brain slice recording in the current study. Our data showing that the TMEM16A inhibitors abolish the MHb CaCC current and suppress MHb LLRP strongly indicate that TMEM16A plays an essential role in sustaining the LLRP. Conditional knockout of TMEM16A in the MHb induces anxiety-related and anhedonic-like behaviors (*18*, *19*). Future characterization of the MHb-specific TMEM16A knockout mice is expected to fully establish TMEM16A as a major driver for the LLRP and dissect its physiological role in modulating nicotine addiction and emotional processes.

Despite the fact that previous studies have shown that the transcripts of *KCNMA1* and its regulatory subunits are highly expressed in the MHb (*15*, *43*, *44*), here we provide the first functional evidence that BK channels are expressed in the MHb. Our pharmacological

and genetic inhibition and potentiation of BK channels using mouse models explicitly demonstrate that BK channels play an important role in regulating the maintenance and termination of the LLRP (Fig. 9, bottom right). Characterizing the responses to nicotine in the *Kcnma1* knockout mice and our BK-D434G GOF channelopathy mice will help further understand the neurological function of MHb BK channels in nicotine addiction and establish if BK channels can be a novel target to prevent nicotine addiction. Although our immunofluorescence experiments detected BK protein expression in the soma (Fig. 8A), the subcellular localization of BK channels in MHb neurons is not clear. On the basis of the known information from other neurons (*56*–*58*), BK channels may express in somatodendritic regions, axons, and pre- and postsynaptic termini, controlling various neuronal activities. It is therefore important to pinpoint the subcellular localizations of MHb BK channels and further dissect their neurological functions in regulating MHb excitability and neurotransmission in response to nicotine and other addictive substances.

In summary, this study reveals a unique, cell-autonomous inhibitory mechanism in MHb neurons, which have unusually high intracellular Cl^- concentrations, causing $GABA_A$ receptors to be excitatory rather than inhibitory. As a result, MHb neurons lack the typical inhibitory mechanisms to suppress hyperexcitability, necessitating alternative regulation, especially in response to nicotine. We found that the MHb's unique LLRP acts as an emergency brake, likely preventing excitotoxicity by using depolarization block until K^+ channels restore membrane potential. Key players in this process include TMEM16A CaCCs, BK Ca^{2+}-activated K^+ channels, and their interaction with the Ca^{2+}-permeable nAChRs and VGCCs. This unconventional mechanism can prevent hyperexcitability from spreading to downstream neurons and offers potential therapeutic targets for nicotine addiction. It would be interesting to further explore whether other neurons, such as immature neurons during development or sensory neurons with high intracellular Cl^- and CaCC expression (*59*–*62*), also use a similar LLRP mechanism to regulate their excitability.

MATERIALS AND METHODS

Mice strains

WT C57Bl/6J mice and ChAT-ChR2-eYFP, BK-KO, and BK-D434G knock-in mice were used in the present study. ChAT-ChR2-eYFP and BK-KO mice were obtained from the Jackson Laboratory (strain no. 014546 and no. 035902, respectively). BK-D434G mutation knock-in mice were recently reported by our group (*45*). Animals were housed at a constant 24°C in a 12-hour light-dark cycle (lights on at 0700) with ad libitum food and water. Both males and females were used for the experiments. Mouse handling and usage were carried out in a strict compliance with a protocol (no. A057–24-02) approved by the Institutional Animal Care and Use Committee at Duke University, in accordance with National Institutes of Health guidelines.

In vivo single-unit recording from MHb

For single-unit recording of the MHb neurons, the implantation surgery was performed with five 2- to 4-month-old mice as previously described (*47*). A craniotomy was executed over the MHb, with coordinates relative to the bregma as follows: 1.46 mm posterior, 0.20 mm lateral, and −2.50 mm ventral. Subsequently, a drivable electrode assembly, comprising a 16-channel recording array encased in a cannula (Innovative Neurophysiology Inc., Durham, NC, USA), was carefully lowered to a position 0.3 mm dorsal to the MHb, reaching a depth of −2.20 mm. To minimize vascular damage and control bleeding, the electrode was angled at 15° from the midline toward the lateral direction, thus circumventing the central cerebral vessel. The single-unit multielectrode array was grounded with a leading wire, which was fixed to the skull (from the bregma: 2.00 mm posterior, 3.00 mm lateral) with a screw. The single-unit electrode array was fixed on the skull by two additional screws followed by superglue and dental cement. After a 7-day recovery, the tips of the single-unit drivable electrodes were advanced 0.3 mm deeper, and the headstage was connected to a preamplifier CerePlex mu headstage (Blackrock Neurotech, Salt Lake, Utah). The single-unit recording from the MHb neurons was recorded by the Blackrock Cerebus data acquisition system (Blackrock Neurotech, Salt Lake, Utah), including the neuronal spike waveform and timestamp. The single-unit recording data were processed by the Offline Sorter x64 V3 (Plexon Inc., Dallas, TX, USA) to sort the single unit through an automatic principal components analysis based on their waveform. The classified single-unit signals were further confirmed manually to exclude the artificial or electrical noise based on their waveforms. The sorted single-unit signals were exported to the NeuroExplorer (Nex Technologies, Colorado Springs, CO 80906, USA) for further analysis.

A custom MATLAB code was used to analyze and depict the alterations in firing frequency of MHb single units under various nicotine injection conditions (https://doi.org/10.7924/r4w95d459). The firing timestamps of these single units were averaged and grouped into 10-s bins. The intraperitoneal injection of saline or nicotine took approximately 10 s and was completed by the 300-s mark. All single-unit traces were aligned at the time of drug administration (the dotted line at 300 s in Fig. 1C). Subsequently, we normalized the firing frequency of any given neuron across the entire recording period against its baseline activity. The baseline was established by averaging the firing frequency 300 s before nicotine administration (0 to 300 s). Postdrug administration (300 to 1200 s) changes in firing frequency—either an increase or decrease >20% relative to the baseline (averaged firing frequency in 0 to 300 s)—were categorized as excitation and inhibition, respectively. For magnified traces from 250 to 400 s (fig. S1, A and B), 1-s time bins of averaged values are shown. The "transient increase of firings" was defined as follows: (i) The sequential change of each time bin was calculated through the entire recordings for all units. (ii) The maximum values of the change within 50 to 100 s (basal) and 300 to 350 s (nicotine) were estimated for each unit. (iii) The transient increase of firings was identified as those in which the change was five times greater than the maximum value of basal. In addition, we conducted a Pearson correlation analysis to examine the relationship between the neuronal population that showed firing frequency increase during low-dose nicotine injection and the neuronal population that showed firing suppression under high-dose nicotine. The stem plots were also created for high-dose nicotine groups using MATLAB code (https://doi.org/10.7924/r4w95d459).

Ex vivo electrophysiology from MHb slice preparation

The recordings were performed using murine brain slices that were acutely prepared as described previously (*45*, *63*). Briefly, animals (postnatal days 15 to 48) were anesthetized with isoflurane and decapitated. Coronal brain slices (250 μm) containing the MHb were

cut in ice-cold N-Methyl-D-glucamine (NMDG) aCSF containing 92 mM NMDG, 2.5 mM KCl, 1.2 mM NaH_2PO_4, 30 mM $NaHCO_3$, 20 mM Hepes, 25 mM glucose, 5 mM sodium ascorbate, 2 mM thiourea, 3 mM sodium pyruvate, 10 mM $MgSO_4$, and 0.5 mM $CaCl_2$ (adjusted pH to 7.4 using HCl). The slices were then incubated in Hepes holding solution containing 92 mM NaCl, 2.5 mM KCl, 1.2 mM NaH_2PO_4, 25 mM $NaHCO_3$, 20 mM Hepes, 25 mM glucose, 5 mM sodium ascorbate, 2 mM thiourea, 3 mM sodium pyruvate, 2 mM $MgSO_4$, and 2 mM $CaCl_2$ (adjusted pH to 7.4 using NaOH) at room temperature for 60 min. After incubation, the slices were transferred to a recording chamber and superfused (3 ml/min) with aCSF at 33°C: 124 mM NaCl, 2.5 mM KCl, 1.2 mM NaH_2PO_4, 24 mM $NaHCO_3$, 5 mM Hepes, 12.5 mM glucose, 2 mM $MgSO_4{\cdot}7H_2O$, and 2 mM $CaCl_2$ (adjusted pH to 7.4 using NaOH). All solutions used for slice preparation were equilibrated with 95% O_2/5% CO_2.

Patch clamp recordings were performed from the ventral medial (MHbVm) and ventral central (MHbVc) part of the MHb (*3*, *64*) using a MultiClamp 700A or 700B amplifier, and the signals were sampled at 2 to 10 kHz using a Digidata1550A A/D converter (Molecular Devices). Data acquisition and analyses were performed using pClamp 10.7 software (Molecular Devices). The extracellular solution used was aCSF, with or without specific ion channel modulators, unless stated otherwise. Focal application of nicotine solutions to the MHb neurons was achieved by locating nicotine-containing pipette near cell body and regulating the air pressure with Picospritzer III (Parker) or Octa-Flow II (ALA Sci.). For LCA recording, aCSF containing pipette was used for the recording. Spontaneous neural activity was detected extracellularly by applying light suction to the cell membrane. The trace was high-pass filtered at 3 Hz to correct the baseline fluctuation.

For whole-cell current clamp recording, pipette resistance was 2 to 5 megohms. In most current clamp recordings, we used 40 mM $[Cl^-]_i$ intracellular solution containing the following: 90 mM K-gluconate, 40 mM KCl, 10 mM Hepes, 2 mM Mg-ATP, 0.3 mM Na_2-GTP, 10 mM disodium phosphocreatine, and 0.2 mM EGTA, adjusted to pH 7.3, with KOH. To vary $[Cl^-]_i$, we adjusted the levels of KCl and K-gluconate based on the 40 mM $[Cl^-]_i$ intracellular solution. In the 80 mM $[Cl^-]_i$ experiment, KCl:K-gluconate ratio was changed to 80 mM:50 mM, respectively.

For whole-cell voltage clamp recording of CaCC current (fig. S2), the intracellular solution contains 110 mM $CsMeSO_3$, 20 mM TEACl, 8 mM KCl, 10 mM Hepes, 2 mM Mg-ATP, 0.3 mM Na_2-GTP, 5 mM QX314-Br, and 0.2 mM EGTA, adjusted to pH 7.3 with CsOH, to inhibit potassium and sodium channels. For nicotine-induced CaCC recordings (Fig. 5, and fig. S3), the "140 mM $[Cl^-]_{in}$" solution contained 140 mM CsCl, 10 mM Hepes, 0.2 mM EGTA, 2 mM Mg-ATP, and 0.3 mM Na_2-GTP. The 5 mM $[Cl^-]_{in}$ solution contained 5 mM CsCl, 135 mM $CsMeSo_3$, 10 mM Hepes, 0.2 mM EGTA, 2 mM Mg-ATP, and 0.3 mM Na_2-GTP. The "140 mM $[Cl^-]_{in}$ + 5 mM $[EGTA]_{in}$" solution contained 140 mM CsCl, 10 mM Hepes, 5 mM EGTA, 2 mM Mg-ATP, and 0.3 mM Na_2-GTP. As shown in Fig. 5, we observed several components in nicotine-induced currents. Instantaneous current (i) was measured at 0.5 s after nicotine application, while a peak growing phase current (ii) was the maximum current between 0.5 and 5 s after nicotine application. The decaying phase (iii) current was calculated by integrating current density for 10 s after terminating the nicotine puff.

When we analyzed the plateau potential, we low-pass filtered the recordings at 3 Hz to remove the action potentials. We defined the plateau potentials with the following definitions: (i) the membrane potential is above −40 mV, (ii) the slope is more than −0.8 mV/s, and (iii) it is longer that 3 s after puff stimulation was finished.

In optogenetic stimulation experiments (Fig. 3), a blue light laser (473 nm) was applied to the MHb neurons from the ChAT-ChR2-eYFP mice through an optogenetic stimulator (Inper, Hangzhou, China). The laser power at the tip of the fiber was adjusted to ~3 mW and the laser stimulation was controlled by pClamp 10.7 (Molecular Devices).

Immunohistochemistry

After anesthetizing with isoflurane, animals were perfused from the heart with 0.75% NaCl, followed by 4% paraformaldehyde (PFA) in phosphate-buffered saline (PBS). The brain was fixed with 4% PFA/PBS at 4°C overnight. The tissues were dehydrated in 30% sucrose/PBS at 4°C overnight. After embedding with optimal cutting temperature compounds, the coronal sections (50 μm) were cut by a cryostat (CM1900, Leica). Sections were incubated with 5% normal goat serum for 2 hours, a primary antibody overnight (Rabbit anti-KCNMA1, APC-021, Alomone, 1:200). After 3 rinses with PBS for 10 min, secondary antibodies (1:1000, conjugated with goat anti-rabbit Alexa 488, Thermo Fisher Scientific, A-11008) were incubated for 2 hours at room temperature. Then, the sections were washed three times with PBS for 10 min each and stained with 4′,6-diamidino-2-phenylindole (DAPI; 1:10,000 of 5 mg/ml, Sigma-Aldrich). Images were acquired using a Zeiss 780 inverted confocal microscope. Representative images were taken from at least three repeats.

Data analysis

Data analyses were performed with Excel 2016 (Microsoft, USA). Statistical analyses were performed with Prism 6 (GraphPad Software, San Diego, CA). For multiple comparisons, we conducted nonparametric tests (Dunn's multiple comparisons) or parametric tests (*t* test with Bonferroni correction or Dunnett's test) as appropriate for comparison of multiple groups. Outliers were identified using the robust regression and outlier removal method (*65*). Data are shown with mean ± SEM unless noted otherwise. Sample sizes were chosen based on field standards. No statistical methods were used to predetermine sample size.

Supplementary Materials

This PDF file includes:

Supplementary Methods
Figs. S1 to S3

REFERENCES AND NOTES

1. GBD 2019 Tobacco Collaborators, Spatial, temporal, and demographic patterns in prevalence of smoking tobacco use and attributable disease burden in 204 countries and territories, 1990-2019: A systematic analysis from the Global Burden of Disease Study 2019. *Lancet* **397**, 2337–2360 (2021).
2. D. C. Perry, Y. X. Xiao, H. N. Nguyen, J. L. Musachio, M. I. Davila-Garcia, K. J. Kellar, Measuring nicotinic receptors with characteristics of α4β2, α3β2 and α3β4 subtypes in rat tissues by autoradiography. *J. Neurochem.* **82**, 468–481 (2002).
3. P. Y. Shih, S. E. Engle, G. Oh, P. Deshpande, N. L. Puskar, H. A. Lester, R. M. Drenan, Differential expression and function of nicotinic acetylcholine receptors in subdivisions of medial habenula. *J. Neurosci.* **34**, 9789–9802 (2014).
4. L. Wills, J. L. Ables, K. M. Braunscheidel, S. P. B. Caligiuri, K. S. Elayouby, C. Fillinger, M. Ishikawa, J. K. Moen, P. J. Kenny, Neurobiological mechanisms of nicotine reward and aversion. *Pharmacol. Rev.* **74**, 271–310 (2022).
5. C. D. Fowler, P. J. Kenny, Nicotine aversion: Neurobiological mechanisms and relevance to tobacco dependence vulnerability. *Neuropharmacology* **76**, 533–544 (2014).
6. C. D. Fowler, Q. Lu, P. M. Johnson, M. J. Marks, P. J. Kenny, Habenular α5 nicotinic receptor subunit signalling controls nicotine intake. *Nature* **471**, 597–601 (2011).
7. Y. Ise, T. Mori, S. Katayama, T. Suzuki, T. C. Wang, Genetic background influences nicotine-induced conditioned place preference and place aversion in mice. *J. Nippon Med. Sch.* **81**, 53–56 (2014).

8. E. J. Popke, A. J. Mayorga, C. M. Fogle, M. G. Paule, Effects of acute nicotine on several operant behaviors in rats. *Pharmacol. Biochem. Behav.* **65**, 247–254 (2000).
9. A. Gorlich, B. Antolin-Fontes, J. L. Ables, S. Frahm, M. A. Slimak, J. D. Dougherty, I. Ibanez-Tallon, Reexposure to nicotine during withdrawal increases the pacemaking activity of cholinergic habenular neurons. *Proc. Natl. Acad. Sci. U.S.A.* **110**, 17077–17082 (2013).
10. K. M. Velasquez, D. L. Molfese, R. Salas, The role of the habenula in drug addiction. *Front. Hum. Neurosci.* **8**, 174 (2014).
11. A. Duncan, M. P. Heyer, M. Ishikawa, S. P. B. Caligiuri, X.-A. Liu, Z. Chen, M. V. M. Di Bonaventura, K. S. Elayouby, J. L. Ables, W. M. Howe, P. Bali, C. Fillinger, M. Williams, R. M. O'Connor, Z. Wang, Q. Lu, T. M. Kamenecka, A. Ma'ayan, H. C. O'Neill, I. Ibanez-Tallon, A. M. Geurts, P. J. Kenny, Habenular TCF7L2 links nicotine addiction to diabetes. *Nature* **574**, 372–377 (2019).
12. S. Frahm, M. A. Slimak, L. Ferrarese, J. Santos-Torres, B. Antolin-Fontes, S. Auer, S. Filkin, S. Pons, J. F. Fontaine, V. Tsetlin, U. Maskos, I. Ibanez-Tallon, Aversion to nicotine is regulated by the balanced activity of β4 and α5 nicotinic receptor subunits in the medial habenula. *Neuron* **70**, 522–535 (2011).
13. A. Tsuzuki, M. Yamasaki, K. Konno, T. Miyazaki, N. Takei, S. Tomita, M. Yuzaki, M. Watanabe, Abundant extrasynaptic expression of α3β4-containing nicotinic acetylcholine receptors in the medial habenula-interpeduncular nucleus pathway in mice. *Sci. Rep.* **14**, 14193 (2024).
14. K. Choi, Y. Lee, C. Lee, S. Hong, S. Lee, S. J. Kang, K. S. Shin, Optogenetic activation of septal GABAergic afferents entrains neuronal firing in the medial habenula. *Sci. Rep.* **6**, 34800 (2016).
15. Y. Hashikawa, K. Hashikawa, M. A. Rossi, M. L. Basiri, Y. Liu, N. L. Johnston, O. R. Ahmad, G. D. Stuber, Transcriptional and spatial resolution of cell types in the mammalian habenula. *Neuron* **106**, 743–758.e5 (2020).
16. D. G. Wang, N. Gong, B. Luo, T. L. Xu, Absence of GABA type A signaling in adult medial habenular neurons. *Neuroscience* **141**, 133–141 (2006).
17. U. Kim, L. Y. Chung, Dual GABAergic synaptic response of fast excitation and slow inhibition in the medial habenula of rat epithalamus. *J. Neurophysiol.* **98**, 1323–1332 (2007).
18. C.-H. Cho, S. Lee, A. Kim, O. Yarishkin, K. Ryoo, Y.-S. Lee, H.-G. Jung, E. Yang, D. Y. Lee, B. Lee, H. Kim, U. Oh, H.-I. Im, E. M. Hwang, J.-Y. Park, TMEM16A expression in cholinergic neurons of the medial habenula mediates anxiety-related behaviors. *EMBO Rep.* **21**, e48097 (2020).
19. J. G. Song, O. Kwon, E. M. Hwang, H. W. Kim, J. Y. Park, Conditional deletion of TMEM16A in cholinergic neurons of the medial habenula induces anhedonic-like behavior in mice. *Behav. Brain Res.* **426**, 113841 (2022).
20. M. Herkenham, W. J. Nauta, Afferent connections of the habenular nuclei in the rat. A horseradish peroxidase study, with a note on the fiber-of-passage problem. *J. Comp. Neurol.* **173**, 123–146 (1977).
21. Y. Otsu, S. Lecca, K. Pietrajtis, C. V. Rousseau, P. Marcaggi, G. P. Dugue, C. Mailhes-Hamon, M. Mameli, M. A. Diana, Functional principles of posterior septal inputs to the medial habenula. *Cell Rep.* **22**, 693–705 (2018).
22. C. Qin, M. Luo, Neurochemical phenotypes of the afferent and efferent projections of the mouse medial habenula. *Neuroscience* **161**, 827–837 (2009).
23. S. P. B. Caligiuri, W. M. Howe, L. Wills, A. C. W. Smith, Y. Lei, P. Bali, M. P. Heyer, J. K. Moen, J. L. Ables, K. S. Elayouby, M. Williams, C. Fillinger, Z. Oketokoun, V. E. Lehmann, A. G. DiFeliceantonio, P. M. Johnson, K. Beaumont, R. P. Sebra, I. Ibanez-Tallon, P. J. Kenny, Hedgehog-interacting protein acts in the habenula to regulate nicotine intake. *Proc. Natl. Acad. Sci. U.S.A.* **119**, e2209870119 (2022).
24. S. D. Grabus, B. R. Martin, S. E. Brown, M. I. Damaj, Nicotine place preference in the mouse: Influences of prior handling, dose and strain and attenuation by nicotinic receptor antagonists. *Psychopharmacology (Berl)* **184**, 456–463 (2006).
25. H. Lee, M. S. Kang, J. M. Chung, J. Noh, Repeated nicotine exposure in adolescent rats: Reduction of medial habenular activity and augmentation of nicotine preference. *Physiol. Behav.* **138**, 345–350 (2015).
26. N. L. Benowitz, Pharmacology of nicotine: Addiction, smoking-induced disease, and therapeutics. *Annu. Rev. Pharmacol. Toxicol.* **49**, 57–71 (2009).
27. J. E. Rose, A. G. Mukhin, S. J. Lokitz, T. G. Turkington, J. Herskovic, F. M. Behm, S. Garg, P. K. Garg, Kinetics of brain nicotine accumulation in dependent and nondependent smokers assessed with PET and cigarettes containing 11C-nicotine. *Proc. Natl. Acad. Sci. U.S.A.* **107**, 5190–5195 (2010).
28. J. Ren, C. Qin, F. Hu, J. Tan, L. Qiu, S. Zhao, G. Feng, M. Luo, Habenula "cholinergic" neurons co-release glutamate and acetylcholine and activate postsynaptic neurons via distinct transmission modes. *Neuron* **69**, 445–452 (2011).
29. S. Zhao, J. T. Ting, H. E. Atallah, L. Qiu, J. Tan, B. Gloss, G. J. Augustine, K. Deisseroth, M. Luo, A. M. Graybiel, G. Feng, Cell type-specific channelrhodopsin-2 transgenic mice for optogenetic dissection of neural circuitry function. *Nat. Methods* **8**, 745–752 (2011).
30. B. Hille, *Ion Channels of Excitable Membranes* (3rd ed.) (2001).
31. H. C. Hartzell, K. Yu, Q. Xiao, L. T. Chien, Z. Qu, Anoctamin/TMEM16 family members are Ca^{2+}-activated Cl^- channels. *J. Physiol.* **587**, 2127–2139 (2009).
32. B. C. Schroeder, T. Cheng, Y. N. Jan, L. Y. Jan, Expression cloning of TMEM16A as a calcium-activated chloride channel subunit. *Cell* **134**, 1019–1029 (2008).
33. A. Caputo, E. Caci, L. Ferrera, N. Pedemonte, C. Barsanti, E. Sondo, U. Pfeffer, R. Ravazzolo, O. Zegarra-Moran, L. J. Galietta, TMEM16A, a membrane protein associated with calcium-dependent chloride channel activity. *Science* **322**, 590–594 (2008).
34. Y. D. Yang, H. Cho, J. Y. Koo, M. H. Tak, Y. Cho, W. S. Shim, S. P. Park, J. Lee, B. Lee, B. M. Kim, R. Raouf, Y. K. Shin, U. Oh, TMEM16A confers receptor-activated calcium-dependent chloride conductance. *Nature* **455**, 1210–1215 (2008).
35. S. C. Le, P. Liang, A. J. Lowry, H. Yang, Gating and regulatory mechanisms of TMEM16 ion channels and scramblases. *Front. Physiol.* **12**, 787773 (2021).
36. N. Pedemonte, L. J. Galietta, Structure and function of TMEM16 proteins (anoctamins). *Physiol. Rev.* **94**, 419–459 (2014).
37. W. Namkung, P. W. Phuan, A. S. Verkman, TMEM16A inhibitors reveal TMEM16A as a minor component of calcium-activated chloride channel conductance in airway and intestinal epithelial cells. *J. Biol. Chem.* **286**, 2365–2374 (2011).
38. R. De La Fuente, W. Namkung, A. Mills, A. S. Verkman, Small-molecule screen identifies inhibitors of a human intestinal calcium-activated chloride channel. *Mol. Pharmacol.* **73**, 758–768 (2008).
39. P. Bhandari, D. Vandael, D. Fernandez-Fernandez, T. Fritzius, D. Kleindienst, C. Onal, J. Montanaro, M. Gassmann, P. Jonas, A. Kulik, B. Bettler, R. Shigemoto, P. Koppensteiner, $GABA_B$ receptor auxiliary subunits modulate Cav2.3-mediated release from medial habenula terminals. *eLife* **10**, e68274 (2021).
40. C. R. Vickstrom, X. Liu, Y. Zhang, L. Mu, T. J. Kelly, X. Yan, M.-M. Hu, S. T. Snarrenberg, Q.-S. Liu, T-type calcium channels contribute to burst firing in a subpopulation of medial habenula neurons. *eNeuro* **7**, doi: 10.1523/ENEURO.0201-20.2020 (2020).
41. H. Berkefeld, B. Fakler, U. Schulte, Ca^{2+}-activated K^+ channels: From protein complexes to function. *Physiol. Rev.* **90**, 1437–1459 (2010).
42. H. Berkefeld, C. A. Sailer, W. Bildl, V. Rohde, J. O. Thumfart, S. Eble, N. Klugbauer, E. Reisinger, J. Bischofberger, D. Oliver, H. G. Knaus, U. Schulte, B. Fakler, BKCa-Cav channel complexes mediate rapid and localized Ca^{2+}-activated K^+ signaling. *Science* **314**, 615–620 (2006).
43. U. Sausbier, M. Sausbier, C. A. Sailer, C. Arntz, H. G. Knaus, W. Neuhuber, P. Ruth, Ca^{2+}-activated K^+ channels of the BK-type in the mouse brain. *Histochem. Cell Biol.* **125**, 725–741 (2006).
44. Y.-Y. Zhang, X. Han, Y. Liu, J. Chen, L. Hua, Q. Ma, Y.-Y.-X. Huang, Q.-Y. Tang, Z. Zhang, mRNA expression of LRRC55 protein (leucine-rich repeat-containing protein 55) in the adult mouse brain. *PLOS ONE* **13**, e0191749 (2018).
45. P. Dong, Y. Zhang, A. S. Hunanyan, M. A. Mikati, J. Cui, H. Yang, Neuronal mechanism of a BK channelopathy in absence epilepsy and dyskinesia. *Proc. Natl. Acad. Sci. U.S.A.* **119**, e2200140119 (2022).
46. W. Du, J. F. Bautista, H. Yang, A. Diez-Sampedro, S. A. You, L. Wang, P. Kotagal, H. O. Luders, J. Shi, J. Cui, G. B. Richerson, Q. K. Wang, Calcium-sensitive potassium channelopathy in human epilepsy and paroxysmal movement disorder. *Nat. Genet.* **37**, 733–738 (2005).
47. P. Dong, K. Bakhurin, Y. Li, M. A. Mikati, J. Cui, W. M. Grill, H. H. Yin, H. Yang, Attenuating midline thalamus bursting to mitigate absence epilepsy. *Proc. Natl. Acad. Sci. U.S.A.* **121**, e2403763121 (2024).
48. S. Passlick, E. R. Thapaliya, Z. X. Chen, M. T. Richers, G. C. R. Ellis-Davies, Optical probing of acetylcholine receptors on neurons in the medial habenula with a novel caged nicotine drug analogue. *J. Physiol.* **596**, 5307–5318 (2018).
49. C. Mulle, D. Choquet, H. Korn, J. P. Changeux, Calcium influx through nicotinic receptor in rat central neurons—Its relevance to cellular-regulation. *Neuron* **8**, 135–143 (1992).
50. C. Hartzell, I. Putzier, J. Arreola, Calcium-activated chloride channels. *Annu. Rev. Physiol.* **67**, 719–758 (2005).
51. O. A. Ghosheh, L. P. Dwoskin, D. K. Miller, P. A. Crooks, Accumulation of nicotine and its metabolites in rat brain after intermittent or continuous peripheral administration of [2'-^{14}C]nicotine. *Drug Metab. Dispos.* **29**, 645–651 (2001).
52. N. G. Ilback, T. Stalhandske, Nicotine accumulation in the mouse brain is age-dependent and is quantitatively different in various segments. *Toxicol. Lett.* **143**, 175–184 (2003).
53. A. Wei, C. Solaro, C. Lingle, L. Salkoff, Calcium sensitivity of BK-type K_{Ca} channels determined by a separable domain. *Neuron* **13**, 671–681 (1994).
54. J. Tien, C. J. Peters, X. M. Wong, T. Cheng, Y. N. Jan, L. Y. Jan, H. Yang, A comprehensive search for calcium binding sites critical for TMEM16A calcium-activated chloride channel activity. *eLife* **3**, e02772 (2014).
55. Y. Otsu, E. Darcq, K. Pietrajtis, F. Mátyás, E. Schwartz, T. Bessaih, S. A. Gerges, C. V. Rousseau, T. Grand, S. Dieudonné, P. Paoletti, L. Acsády, C. Agulhon, B. L. Kieffer, M. A. Diana, Control of aversion by glycine-gated GluN1/GluN3A NMDA receptors in the adult medial habenula. *Science* **366**, 250–254 (2019).
56. H. Hu, L. R. Shao, S. Chavoshy, N. Gu, M. Trieb, R. Behrens, P. Laake, O. Pongs, H. G. Knaus, O. P. Ottersen, J. F. Storm, Presynaptic Ca^{2+}-activated K^+ channels in glutamatergic

hippocampal terminals and their role in spike repolarization and regulation of transmitter release. *J. Neurosci.* **21**, 9585–9597 (2001).
57. C. A. Sailer, W. A. Kaufmann, M. Kogler, L. Chen, U. Sausbier, O. P. Ottersen, P. Ruth, M. J. Shipston, H. G. Knaus, Immunolocalization of BK channels in hippocampal pyramidal neurons. *Eur. J. Neurosci.* **24**, 442–454 (2006).
58. W. A. Kaufmann, F. Ferraguti, Y. Fukazawa, Y. Kasugai, R. Shigemoto, P. Laake, J. A. Sexton, P. Ruth, G. Wietzorrek, H. G. Knaus, J. F. Storm, O. P. Ottersen, Large-conductance calcium-activated potassium channels in purkinje cell plasma membranes are clustered at sites of hypolemmal microdomains. *J. Comp. Neurol.* **515**, 215–230 (2009).
59. Y. Takayama, D. Uta, H. Furue, M. Tominaga, Pain-enhancing mechanism through interaction between TRPV1 and anoctamin 1 in sensory neurons. *Proc. Natl. Acad. Sci. U.S.A.* **112**, 5213–5218 (2015).
60. T. Kurahashi, K. W. Yau, Co-existence of cationic and chloride components in odorant-induced current of vertebrate olfactory receptor cells. *Nature* **363**, 71–74 (1993).
61. S. Mao, T. Garzon-Muvdi, M. Di Fulvio, Y. Chen, E. Delpire, F. J. Alvarez, F. J. Alvarez-Leefmans, Molecular and functional expression of cation-chloride cotransporters in dorsal root ganglion neurons during postnatal maturation. *J. Neurophysiol.* **108**, 834–852 (2012).
62. H. Kaneko, T. Nakamura, B. Lindemann, Noninvasive measurement of chloride concentration in rat olfactory receptor cells with use of a fluorescent dye. *Am. J. Physiol. Cell Physiol.* **280**, C1387–C1393 (2001).
63. D. C. Perry, Y. Xiao, H. N. Nguyen, J. L. Musachio, M. I. Dávila-García, K. J. Kellar, Preparation of acute brain slices using an optimized N-methyl-D-glucamine protective recovery method. *J. Vis. Exp.* , 53825 (2018).
64. F. Wagner, T. Stroh, R. W. Veh, Correlating habenular subnuclei in rat and mouse by using topographic, morphological, and cytochemical criteria. *J. Comp. Neurol.* **522**, 2650–2662 (2014).
65. H. J. Motulsky, R. E. Brown, Detecting outliers when fitting data with nonlinear regression—A new method based on robust nonlinear regression and the false discovery rate. *BMC Bioinformatics* **7**, 123 (2006).
66. Y. Zhang, Z. Zhang, S. Xiao, J. Tien, S. Le, T. Le, L. Y. Jan, H. Yang, Inferior olivary TMEM16B mediates cerebellar motor learning. *Neuron* **30**, 1103–1111.e4 (2017).

Acknowledgments: We thank Y. Okamura (Osaka University) for making this collaborative project possible. **Funding:** This work was supported by the Holland-Trice Scholars Award (to H.Y.), the US-Japan Brain Research Cooperative Program (to T.K.), and the Grant-in-Aid for Fund for the Promotion of Joint International Research [Fostering Joint International Research(A) to T.K.]. **Author contributions:** Conceptualization: H.Y., P.D., and T.K. Investigation: T.K. and P.D. Methodology: H.Y., H.H.Y., T.K., P.D., and K.B. Software: P.D. and H.H.Y. Validation: T.K., P.D., H.H.Y., and H.Y. Formal analysis: T.K., P.D., K.B., and H.H.Y. Resources: H.Y. and H.H.Y. Data curation: H.Y. Writing—original draft: H.Y., T.K., and P.D. Writing—review and editing: All authors. Visualization: T.K., P.D., and H.H.Y. Supervision: H.Y. Project administration: H.Y. Funding acquisition: H.Y. and T.K. **Competing interests:** The authors declare that they have no competing interests. **Data and materials availability:** All data needed to evaluate the conclusions in the paper are present in the paper and/or the Supplementary Materials. All relevant codes supporting the present study are available at https://doi.org/10.7924/r4w95d459 or GitHub: https://github.com/superdongping/MHb_nicotine.

Submitted 5 May 2024
Accepted 10 February 2025
Published 19 March 2025
10.1126/sciadv.adq2629